Universiteit
Leiden
The Netherlands

Studying dark matter haloes with weak lensing

Velander, M.B.M.

Citation
Velander, M. B. M. (2012, June 20). *Studying dark matter haloes with weak lensing*. Retrieved from https://hdl.handle.net/1887/19107

Version:	Corrected Publisher's Version
License:	Licence agreement concerning inclusion of doctoral thesis in the Institutional Repository of the University of Leiden
Downloaded from:	https://hdl.handle.net/1887/19107

Note: To cite this publication please use the final published version (if applicable).

Cover Page

Universiteit Leiden

The handle http://hdl.handle.net/1887/19107 holds various files of this Leiden University dissertation.

Author: Velander, Malin Barbro Margareta
Title: Studying dark matter haloes with weak lensing
Issue Date: 2012-06-20

Introduction 1

The vast unknown that is our Universe has always fascinated mankind. Though science is progressing fast and efficiently, still a large number of riddles remain unsolved. Every decade brings with it new discoveries, but more often than not a breakthrough gives rise to yet more questions. Amongst the main advancements of the past quarter-century is the uncovering of dark matter and dark energy as the principal ingredients of our standard model of cosmology. With this model our understanding of the mechanisms behind the origin and the evolution of our Universe has progressed immensely, but to advance further we have do answer this: what is dark matter and dark energy? To help bring clarity to the nature of these phenomena we study the distribution of matter within galaxies, within galaxy clusters, and throughout our Universe. A relatively recent technique, developed in the last couple of decades, has the ability to map matter regardless of whether it is visible or dark and without it having to be confined to large overdensities such as galaxy clusters. This technique is known as *weak gravitational lensing* and it is a highly powerful probe of cosmology.

With this Thesis I aim to increase our knowledge of the distribution of matter in galaxies and galaxy clusters both by further developing the theoretical framework for weak lensing, and by using large optical surveys to observe the weak lensing signal directly. I therefore start with a brief introduction to cosmology and to gravitational lensing, with an emphasis on weak lensing and the current status of lensing distortion software.

1.1 Cosmology

1.1.1 The concordance model of cosmology

Cosmologists study the Universe as a whole and are striving to understand how it was formed and how it has arrived at the point where we are now. How did the initially nearly smooth and homogeneous matter distribution evolve to form the stars, galaxies and galaxy clusters that surround us today? To describe this process we use a template which we know to be a fairly accurate description of reality. The one currently favoured by cosmologists is known as ΛCDM, where Λ represents *dark energy* and CDM stands for *cold dark matter*. This model attempts to simultaneously explain the growth of matter structure

observed throughout the Universe, the temperature structure observed in the cosmic microwave background (CMB), and the accelerated expansion of the Universe indicated by e.g. supernova studies. In the process ΛCDM quantifies the size of the mass-energy density constituents. Surprisingly, the known components of the Standard Model of Particle Physics, such as electrons, protons and neutrons, compose only a minor part — about 5% — while the majority of the matter constituents appears to be something new: dark matter. Even more surprising is that the majority of the energy density appears to be composed of the mysterious dark energy which makes up some 70% of the total. Dark matter is necessary for structure formation as it adds gravity which holds large structures such as galaxies or clusters of galaxies together. Though we have not yet determined exactly what dark matter is, there are some indications of what it could possibly be. Traditionally there are three categories of dark matter: *cold*, *warm* and *hot*. These labels refer to how fast the particles were able to move at the very beginning of the Universe. Cold dark matter became non-relativistic early on, while hot dark matter stayed relativistic until shortly before the epoch known as recombination during which atoms formed. Since we know the temperature of the Universe at that time, this also sets limits on the masses of such particles, with hot dark matter being much lighter than cold dark matter. The most commonly known candidate for a hot dark matter particle is the neutrino. Neutrinos are very light and conform to the constraint that dark matter has to be only *weakly interacting*, making them hard to detect. A model dominated by hot dark matter is inconsistent with hierarchical galaxy formation though, so this alternative has effectively been ruled out via observations. Warm dark matter is then more feasible, and behaves similarly to cold dark matter on large scales though there may be differences on small scales. The most commonly considered candidate warm dark matter particle is the sterile neutrino which is more massive than its hot dark matter counterpart. However, since these sterile neutrinos are not well motivated in particle physics, the current standard model of cosmology prefers cold dark matter. There is now a plethora of candidates for what cold dark matter could be since there is no real upper limit to the mass allowed. Thus these candidates range from the hypothetical *weakly interacting particles* (WIMPs), which may be massive neutrinos or so-called axions, to *massive compact halo objects* (MACHOs) which could refer to dwarf planets or black holes. Observations have, however, ruled out MACHOs as the sole explanation for dark matter (see e.g. Section 1.2.2) and so it is generally concluded that dark matter must be a new type of cold particle, yet to be discovered. The nature of dark energy requires some further introduction and is therefore discussed later in this Section.

ΛCDM has gained great support due to its ability to successfully reproduce a universe much like ours. Of the triumphs of the model, the results from the Cosmic Background Explorer (COBE; Mather, 1982; Gulkis et al., 1990; Mather et al., 1990) and its successor the Wilkinson Microwave Anisotropy Probe (WMAP; Bennett et al., 2003; Spergel et al., 2003; Jarosik et al., 2011) stand out. The two space missions have together accumulated 15 years' worth of CMB data, producing exceedingly accurate measurements of the echoes of the Big Bang via the CMB angular power spectrum, shown in Figure 1.1. The best-fit model, assuming ΛCDM, is also shown in the Figure, clearly demonstrating that ΛCDM describes current cosmological observations well. This is just one example of ways to constrain cosmology though. Another very powerful probe is

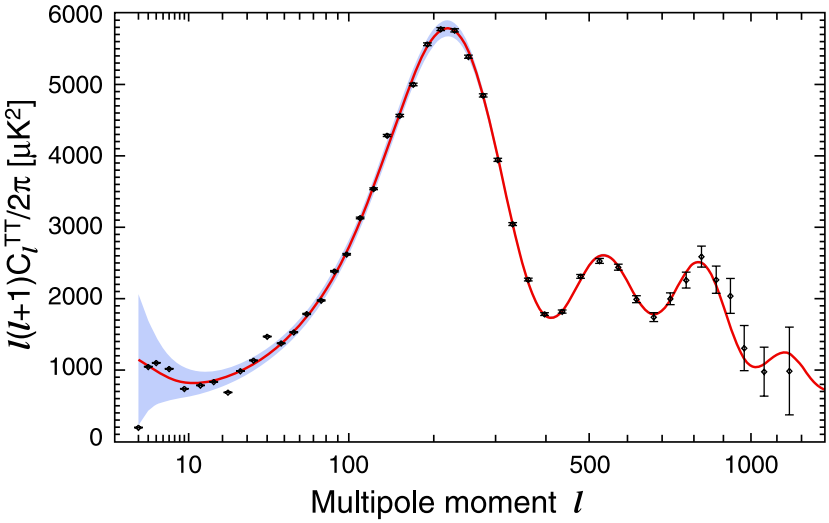

Figure 1.1 The CMB angular power spectrum from the 7-year WMAP data release. The red curve represents the best-fit ΛCDM model and the grey band shows the cosmic variance expected for that model. The first, second and third acoustic peaks are highly constrained. Figure originally published in Larson et al. (2011).

weak lensing which will be introduced later, and yet more probes are discussed in Section 1.1.3.

Selected best-fit parameters from the WMAP 7-year data release are quoted in Table 1.1 and this is also the cosmology assumed throughout this Thesis unless explicitly stated otherwise. These are the aspects of ΛCDM that are relevant to weak gravitational lensing, which is the focus of this work. Conversely, weak gravitational lensing can be used to constrain most of these parameters. To elaborate on the meaning of the parameters in Table 1.1, further background is needed.

Our Universe is expanding which means that objects that are not gravitationally bound together will move away from each other. Therefore we see galaxies and galaxy clusters receding from us in all directions and the further away from us an object is, the faster it moves away from us. The *Hubble constant* H_0 relates this recessional speed to the distance from us via Hubble's Law:

$$v = H_0 D \tag{1.1}$$

The exact value of the Hubble constant is important for interpreting all cosmological results since it affects distances and thus volumes and densities. In most applications, the dimensionless version of the Hubble parameter, h, is used, and it is defined as

$$H_0 \equiv 100\ h\ \mathrm{km\,s^{-1}\,Mpc^{-1}} \tag{1.2}$$

so for the value of H_0 given in Table 1.1 we have $h \simeq 0.70$. Furthermore, objects that are moving away from us will have an electromagnetic spectrum which is shifted towards the redder end due to a stretching of light waves (known as the Doppler effect), and thus we can determine the distance to a distant object via

Table 1.1 Cosmological parameters from the WMAP 7-year data release (Jarosik et al., 2011). These parameters are the result of combining WMAP data with priors from baryonic acoustic oscillations based on the Sloan Digital Sky Survey Data Release 7 (Percival et al., 2010) and from the present-day Hubble constant value determined using 240 Cepheid variables and as many supernovae type Ia (Riess et al., 2009).

Parameter	WMAP7+BAO+H_0 value	Comment
H_0	$70.4^{+1.3}_{-1.4}$ km s^{-1} Mpc^{-1}	The Hubble constant
Ω_b	0.0456 ± 0.0016	Baryon density
Ω_{dm}	0.227 ± 0.014	Dark matter density
Ω_Λ	$0.728^{+0.015}_{-0.016}$	Dark energy density
σ_8	0.809 ± 0.024	Fluctuation amplitude at $8h^{-1}$ Mpc
w	-0.980 ± 0.053	Equation of state

its *redshift* z:

$$1 + z = \frac{\lambda_{\rm obs}}{\lambda_{\rm emit}} \tag{1.3}$$

where $\lambda_{\rm obs}$ and $\lambda_{\rm emit}$ are the observed and emitted wavelengths respectively. Cosmologists often use redshift as a measure of distance to objects, and also — somewhat confusingly — as a measure of time.

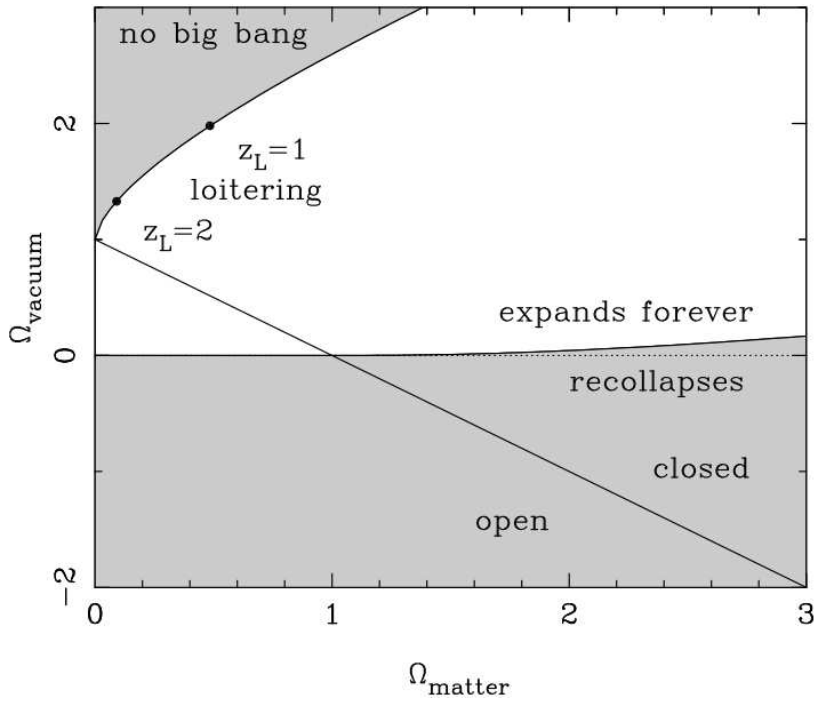

Figure 1.2 Influence of the two main energy density parameters on the overall behaviour of the Universe. Here, $\Omega_{\rm matter}$ and $\Omega_{\rm vacuum}$ are identical to the Ω_m and Ω_Λ parameters mentioned in the text. Figure originally published in Peacock (1999).

We can define a *critical density* $\rho_{\rm crit}$ at time t for which the local Universe is *flat*, i.e. where the angles of a triangle add up to 180°, as

$$\rho_{\rm crit}(t) = \frac{3H^2(t)}{8\pi G} \tag{1.4}$$

Note here that the H parameter is time-dependent; this is the *Hubble parameter* which defines the relative expansion rate at that point in time, and $H_0 \equiv H(t_0)$. G is the gravitational constant. Using this we can then derive a *density parameter* Ω_X which represents the ratio of the actual density to the critical density:

$$\Omega_X = \frac{\rho_X}{\rho_{\rm crit}} = \frac{8\pi G\rho}{3H^2(t)} \tag{1.5}$$

where the subscript X can represent any mass-energy density constituent. Ω_b, Ω_{dm} and Ω_Λ are then the density of baryons, dark matter and dark energy compared to the critical density, and these constants evolve with time and therefore with redshift. Adding the two first parameters together we get the total matter density $\Omega_m = \Omega_b + \Omega_{dm}$. The influence of these parameters on the global behaviour of the Universe is illustrated in Figure 1.2. The solid straight line for which $\Omega_{\rm tot} = \Omega_m + \Omega_\Lambda = 1$ represents a flat universe. For $\Omega_{\rm tot} > 1$ the model is spatially *closed* which means that it has a finite volume and positive curvature everywhere, i.e. the angles of a triangle add up to more than 180° like on the surface of a sphere. Conversely, for $\Omega_{\rm tot} < 1$ the Universe is spatially *open*, has infinite volume and negative curvature everywhere. This type of universe is usually illustrated by a saddle-like shape. Figure 1.2 also shows that a negative Ω_Λ causes the Universe to eventually recollapse while it will continue to expand forever for a positive parameter (in most cases). There is also the possibility of a 'loitering' model with a maximum redshift and infinite age, and for high values of Ω_Λ there is no Big Bang. The current parameter estimates thus support a flat universe which will be expanding forever. We can write the Hubble parameter in terms of density parameters and redshifts:

$$H^2(a) = H_0^2\left[\Omega_\Lambda + \Omega_m a^{-3} + \Omega_r a^{-4} - (\Omega_{\rm tot} - 1)a^{-2}\right] \tag{1.6}$$

where $a = 1/(1+z)$ is a scale factor, Ω_r is the density of radiation energy and $\Omega_{\rm tot}$ is equal to 1 for a spatially flat Universe. All density parameters are defined at the present time, t_0.

The next parameter in Table 1.1, σ_8, is a crucial parameter for cosmology. Formally it is the fluctuation amplitude within a sphere of radius $8\,h^{-1}$ Mpc and functions as a normalisation for the linear matter power spectrum. The value of this parameter influences the growth of structure in the Universe. If it is too low, the fluctuations in the early Universe were too small to feasibly allow for the formation of the stars and galaxies we see today. Finally, the parameter $w \equiv p/\rho c^2$, where p is pressure, defines the equation of state of a postulated contribution to the overall energy density from an unknown quantity. For $w \simeq -1$ this quantity causes an accelerated expansion and the Universe is thus expanding at an ever-increasing rate due to some unknown energy contribution, commonly referred to as dark energy. The presence of this dark energy has been corroborated via several observational indicators of an accelerated expansion (see Section 1.1.3). Just as for dark matter, we have yet to confirm the exact nature of dark energy, though candidates may be categorised as either a constant homogeneous energy

density or *scalar fields* which may vary through space-time. The scalar fields alternative is discussed further in the next Section, but the concordance model ΛCDM assumes a constant energy density which is represented by the cosmological constant Λ. The use of this particular constant is a nod to Einstein and his attempt to balance his field equations to obtain a static universe. Though Einstein's exact solution has since been proven unstable, the recycling of his constant to represent an accelerating universe signifies the similarities between his constant and the behaviour of modern dark energy.

1.1.2 Alternative models

Although ΛCDM is generally accepted as the most successful model for describing our Universe given current observations, there are alternative descriptions. One of the main criticisms of ΛCDM is the need for unknown 'dark' quantities and this has been the motivation for the development of alternatives. ΛCDM assumes in general that the laws of physics hold true throughout the Universe. A family of alternative models reason that this assumption may be false and that laws of gravity require modifying at large distances. Amongst the most well-known are *Modified Newtonian Dynamics* (MOND; Milgrom, 1983) and *Tensor-Vector-Scalar gravity* (TeVeS; Bekenstein, 2004).

MOND was initially introduced as a way to model the flat rotation curves of galaxies without the need for dark matter. The puzzle of galaxy rotation curves was first noted by Rubin & Ford (1970). Studying the Andromeda galaxy, they found that the velocities of stars in the disk stayed constant rather than decreased with distance as would be expected from classical mechanics. The stars in the outer regions of the disk were thus moving much faster around the centre of the galaxy than should be possible. Freeman (1970) noted a similar behaviour in their sample of disk galaxies, tentatively suggesting that there is undetected matter beyond the optical extent of NGC 300. Rubin et al. (1980) then used a larger galaxy sample to conclude, inspired by a remarkable prediction by Zwicky (1933), that there must be a significant amount of unseen mass beyond the limit of the optical observations. The work of Vera Rubin and colleagues on galaxy rotation curves thus constitutes the first real evidence for dark matter — or an indication that classical mechanics is an inaccurate description on galaxy scales. As the name implies, MOND modifies Newtonian dynamics by allowing for some critical acceleration a_0 below which the classical Newtonian force-acceleration relation, $F \propto a$, breaks down. The acceleration close to massive structures thus obeys general relativity, but at large enough distances force is related to acceleration via $F \propto a^2/a_0$. This theory has been highly successful in modelling the rotation curves of galaxies, particularly for galaxies with low surface brightness which represent an extreme where ΛCDM is currently not as powerful. However, on a galaxy cluster scale MOND still requires more mass than what is observed in baryonic form, with massive neutrinos being suggested as a possibility (Sanders, 2007). Furthermore, because MOND is non-relativistic it cannot reproduce gravitational lensing, or indeed cosmology as a whole and is unable to model the CMB power spectrum. TeVeS was then developed as a relativistic generalisation of MOND and successfully models phenomena that MOND does not. It can reproduce the first and second acoustic peaks in the observed CMB power spectrum shown in Figure 1.1, though this necessitates the inclusion of massive neutrinos (McGaugh, 2004;

Skordis et al., 2006). For the tertiary and higher peaks, the amplitude is too low even with added neutrinos because a baryon-only model necessarily predicts that the peak amplitudes should be monotonically decreasing. As for MOND, TeVeS is also relatively successful in modelling spherically symmetric clusters, although again massive neutrinos are required for an essential dark halo and the neutrino mass necessary is unrealistically large (Takahashi & Chiba, 2007). Merging clusters, a few cases of which are discussed in Section 1.3.4, also pose a problem.

MOND and TeVeS have primarily been developed as an alternative to dark matter rather than attempting to replace the full ΛCDM description which includes considerations of the accelerated expansion of the Universe. Though there has been some work on the acceleration implied in TeVeS (Zhao, 2007; Hao & Akhoury, 2009), further exploration is needed in this area. Other models have been suggested as an alternative to the cosmological constant Λ as mechanisms for accelerating the expansion of the Universe. Amongst the first alternative explanations to be suggested is *quintessence* — a fifth fundamental force which is repulsive. Evolved from string theory, another intriguing model is that of the brane cosmology. *Brane* here is short for membrane, and in this cosmology space-time as we know it is confined to a brane embedded in a higher-dimensional space known as the *bulk*. The fundamental forces of nature are localised to the brane while gravitational force is not, which means that our brane can interact gravitationally with the bulk and with other branes. In one version of brane theory, the Big Bang is the result of a collision between two parallel branes (Khoury et al., 2001). The flavour that has gained most support are the Randall-Sundrum models which assume a five-dimensional space in total, i.e. only one extra dimension for the bulk (Randall & Sundrum, 1999a,b,c). The fifth dimension is finite and there are two branes in the model, although in one version one of the two branes is placed infinitely far away, effectively leaving a sole brane in the model. The energies of the two branes cause a severe warping of spacetime along the fifth dimension. An effective cosmological constant is the automatic result of this model (Cline et al., 1999).

Developing alternative methods to describe our Universe is ultimately beneficial to science because they do further our insight into physical mechanisms, though a completely satisfactory version has yet to emerge. ΛCDM is currently the model that is most successful at recovering what we see in observations on a large range of scales and for many different types of structure. It has to be kept in mind, however, that it is just a model and that it, too, has applications which are not completely understood. Emphasis should also be put on the fact that dark matter and dark energy are just descriptors for gravitational and accelerating fields which help us visualise these fields. Whether the forces involved are due to actual dark particles or due to as yet unknown physics, the effect is the same. And there is a lot of work to be done still before we can claim to fully understand the Universe we live in. The probes of cosmology described below are therefore vital for furthering that understanding.

1.1.3 Cosmology probes

There are several ways to test and constrain our cosmology models and often each such probe is more sensitive to some parameters than others. Combining several datasets will therefore result in much tighter constraints on cosmology

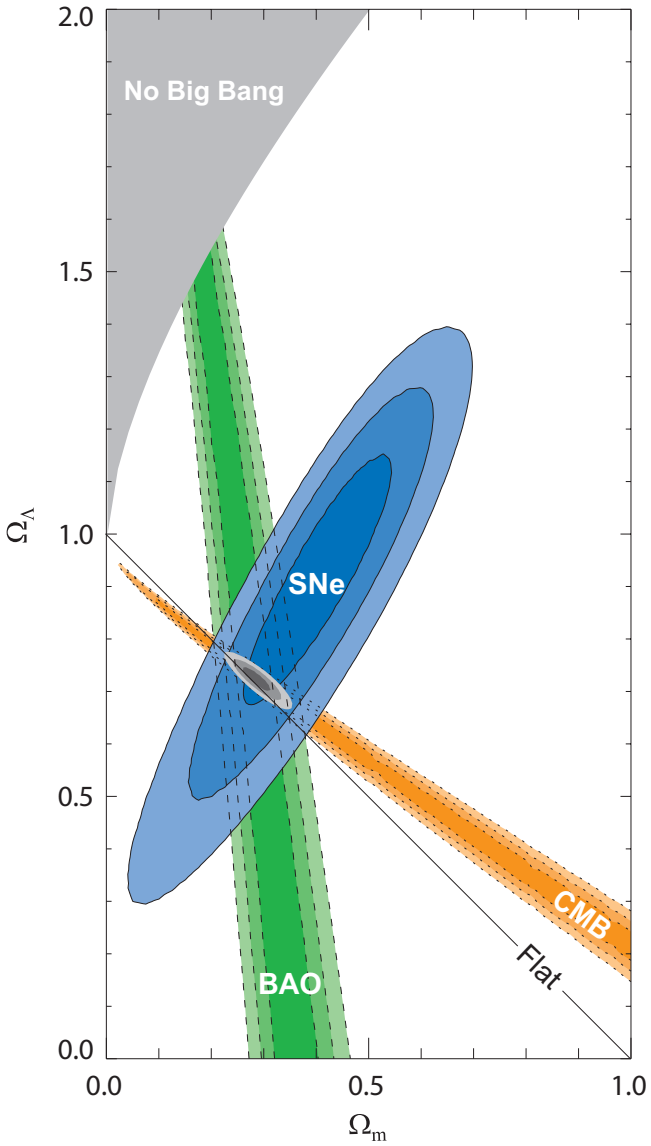

Figure 1.3 Combining several independent datasets to constrain cosmology (c.f. Figure 1.2). The datasets shown in this figure are the results from the cosmic microwave background (CMB; Dunkley et al., 2009), baryon acoustic oscillations (BAO; Eisenstein et al., 2005) and supernovae (SNe; Kowalski et al., 2008). Though each dataset is degenerate in some sense, combining them all gives tight constraints on Ω_m and Ω_Λ (contours at intersection). Figure originally published in Kowalski et al. (2008).

than each on its own.

The CMB power spectrum is sensitive in shape, peak location and relative peak heights to the underlying cosmology (see Figure 1.1, and e.g. Hu & White, 1996; Peacock, 1999). The location of the first acoustic peak is related to the

curvature of the Universe; we now know that the Universe is essentially flat. Furthermore, the location of each peak relative to the previous one is an indicator of the nature of the primordial density perturbations. The peak locations measured by WMAP provide strong support for dark energy. Regarding amplitudes, the amplitude of the first peak compared to the second one (or odd peaks versus even ones) holds information on the baryon density. The more baryons present, the more relatively suppressed the second peak is. Finally, by determining the height of the third peak we determine the ratio of dark matter density to radiation density, and since we know the radiation density from other measurements it gives us the dark matter density in the Universe. However, different parameters may affect the power spectrum in a similar way, which means that we cannot tell whether the shift in one direction is due to the variation of one parameter or another. This is what is known as a *parameter degeneracy*. As an example, the Ω_m and H_0 parameters are degenerate which is why the spread in allowed values for Ω_m is so large (see Figure 1.3). To break such a degeneracy, independent measurements of H_0 are needed and these measurements may be provided by e.g. studies of supernovae (SNe).

Historically, SNe provided one of the first indications of an accelerated expansion (Riess et al., 1998; Perlmutter et al., 1999). SNe is a collective name for all types of stars exploding during, or at the end of, their life cycle. There are several mechanisms that can cause such an explosion, but for cosmological applications one mechanism is of particular interest: that which leads to a Type Ia SN. This species inevitably results in a characteristic light curve, i.e. how the luminosity resulting from the explosion decays with time is identical for all SNe of a given brightness. By precisely measuring such a light curve and comparing it to the observed brightness, the distance to the SN can be accurately inferred. The redshift of the SN host galaxy is then used to constrain the relationship between distance and redshift which in turn constrains Ω_m and Ω_Λ, breaking the degeneracy in the CMB power spectrum as described above (again, see Figure 1.3).

Another probe which allows the breaking of the above degeneracy is the study of large-scale structure (LSS). The way galaxies are distributed throughout the observable Universe is a measure of how matter is distributed and how it clusters, something which is sensitive to Ω_m. Galaxies have therefore been mapped in redshift space through spectroscopic surveys such as the Two-Degree-Field Galaxy Redshift Survey (2dFGRS; see e.g. Cole et al., 2005, for results from the final data set) and the Sloan Digital Sky Survey (SDSS; see e.g. Tegmark et al., 2004). However, because we do not know exactly how the locations of galaxies correspond to the location of the underlying dark matter, interpreting the results in terms of Ω_m is difficult. It requires a description of how well galaxies trace the total mass distribution, and this description is quantified via the *galaxy bias*. The choice of bias constitutes an uncertainty in LSS measurements and needs to be further investigated. In general though, we see a pattern of clustered matter and filaments connecting the clusters, and between the filaments we see voids where there is no matter. This pattern is commonly known as the *Cosmic Web* and the voids are a signature of sound waves created by cosmological matter perturbations in the early Universe, identified as baryon acoustic oscillations (BAO). The imprint of BAO on the matter power spectrum provides a characteristic length scale, and measuring it constrains the distance-redshift relation giving a measure of Ω_m (e.g. Eisenstein et al., 2005,

as in Figure 1.3).

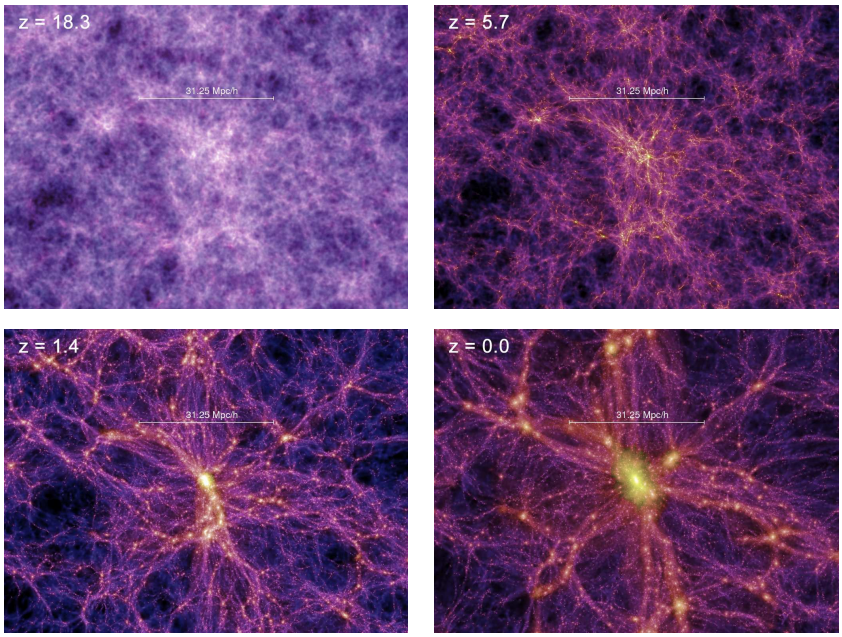

Figure 1.4 Millennium simulation slices at progressively lower redshifts as printed on each panel. The scale of all slices is the same. Images originally published in conjunction with Springel et al. (2005).

A different approach to studying cosmology is to create a new cosmos using the physical laws and properties we are aware of so far. This can be done using so-called *N-body simulations* which take (dark) matter particles, place them according to some initial conditions and let them interact over the life-span of the Universe. Comparing these simulations at different points in redshift to real observations at the same redshifts tells us how well we have understood the underlying physical processes. Currently, the most widely known and used N-body simulation is that of the Millennium Simulation (Springel et al., 2005). Shown in Figure 1.4 are four slices from this dark matter only simulation at different redshifts which illustrate the growth of structure from a nearly homogeneous matter distribution at $z = 18.3$ to a galaxy cluster at $z = 0.0$. One application of N-body simulations is, for instance, that the density profile of a simulated cluster may be modelled and then compared to an equivalent observed cluster studied using gravitational lensing, a technique with the power to map the full mass distribution, to see how well the profiles agree. Studying clusters at different redshifts allows us to investigate the evolution of structure as well. A significant limitation of most N-body simulations is, however, that they use only dark matter particles and disregard the influence of baryons. The reason for this is partly that baryons are expected to follow the general distribution of dark matter and partly that the processes involved are less well understood. The comparison with lensing observations, which are sensitive to all mass, may therefore be somewhat restricted but may also inform us of how the inclusion of baryons affects the dark matter only Universe. This is far from the sole appli-

cation of gravitational lensing in the context of cosmology, and so the technique will be more extensively discussed in the next Section.

1.2 Gravitational lensing overview

Gravitational lensing is the collective name given to a set of methods, all of which have a common goal: to probe gravitational fields irrespective of whether their source is visible or not. In some cases gravitational lensing is the only way to detect what cannot be seen directly through telescopes. As such, the methods are beneficial to the study of the dark components of our Universe discussed in Section 1.1, as well as to the search for extrasolar planets otherwise drowned in the flux of their surroundings.

In essence, gravitational lensing methods exploit the bending of light rays caused by gravitational potentials. As the light travelling from background sources gets *lensed* by foreground structures, the source appears displaced, magnified and distorted. Since this is a purely geometrical effect and since it depends only on the total amount of matter in the intervening structure, no assumptions on the physical state of the lens need be made. This makes gravitational lensing exceedingly powerful.

1.2.1 Fundamentals of lensing

Before elaborating on the different applications of gravitational lensing, the fundamental ideas have to be understood. Here I give a brief introduction to the different concepts involved; for a more in-depth review I refer the reader to Bartelmann & Schneider (2001). The general geometry of gravitational lensing is illustrated in Figure 1.5, and this simple image turns out to represent reality well. The light from a background *source* is deflected by a foreground structure which acts as a *lens*. A customary simplification of this theory is that of the *thin lens approximation*: the light ray is instantaneously deflected at the lens plane. Though this is not strictly correct, it is a valid assumption if the spread of the lensing mass along the line-of-sight is much smaller than the angular diameter distances involved, something which is true in most lensing systems (though for the cosmic mass distribution a more general description is necessary; see Section 1.3.2). As is clear from Figure 1.5, the source image appears displaced with respect to its true position as a result of gravitational lensing. Unfortunately it is difficult to take advantage of this effect observationally since the intrinsic position is not known. However, deflection angle $\hat{\boldsymbol{\alpha}}$ is related to the impact parameter $\boldsymbol{\xi}$ via

$$\hat{\boldsymbol{\alpha}} = \frac{4GM}{c^2\boldsymbol{\xi}} \tag{1.7}$$

where G is the gravitational constant, M is the mass of the lens and c is the speed of light. Thus the amount of deflection is determined not only by the lens mass but also by the impact parameter and this results in a distortion. In extreme geometrical setups where the source is perfectly aligned to lie right behind the lens, the image will be circular. This is known as an *Einstein Ring*, the radius of which is known as the *Einstein radius* θ_E which is directly related

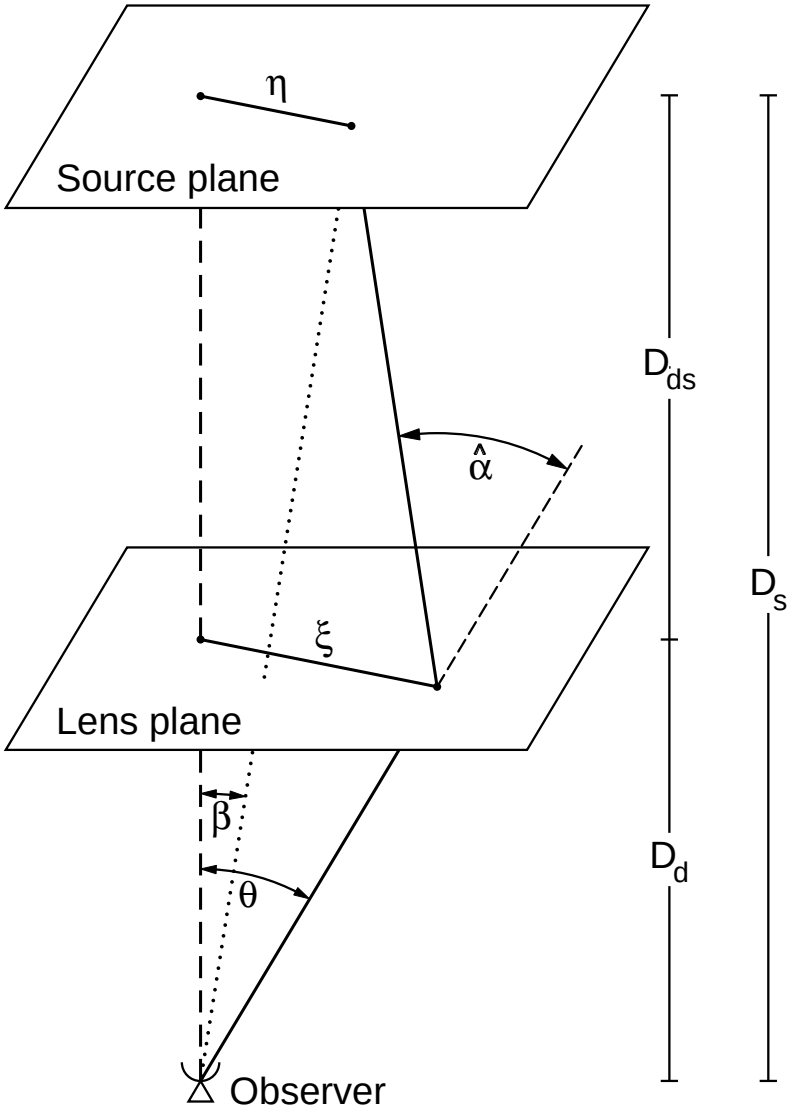

Figure 1.5 Schematic of a typical gravitational lens system. A light ray travelling from a source at position η is deflected by a lens in the lens plane. If there was no lens the source would have been observed at angle β. In the presence of a lens, however, the deflection angle is $\hat{\boldsymbol{\alpha}}$ with the impact parameter $\boldsymbol{\xi}$ which results in the source being observed at angle θ instead. D_s, D_d (D_l in the text) and D_{ds} (D_{ls}) are the angular diameter distances to the source, to the lens and between the lens and the source respectively. Figure originally published in Bartelmann & Schneider (2001).

to the mass of the lens; for a point mass it is given by

$$\theta_E = \frac{D_{ls}}{D_l D_s} \frac{4GM}{c^2} \tag{1.8}$$

We can now define the *lensing equation*:

$$\boldsymbol{\beta} = \boldsymbol{\theta} - \boldsymbol{\alpha}(\boldsymbol{\theta}) \tag{1.9}$$

This basic equation relates the observed position angle $\boldsymbol{\theta} = \boldsymbol{\xi}/D_l$ to the true position $\boldsymbol{\beta}$ and the reduced deflection angle $\boldsymbol{\alpha} = \hat{\boldsymbol{\alpha}} D_{ls}/D_s$. Furthermore, the thin lens approximation allows us to assume that the lensing mass lies on a 2D lens plane and we can therefore define the 2D surface mass density $\Sigma(\boldsymbol{\xi})$ of the lens

$$\Sigma(\boldsymbol{\xi}) = \int \rho(\boldsymbol{\xi}, z)\, \mathrm{d}z \tag{1.10}$$

where ρ is the 3D mass density and z is the third dimension. Now, the lensing equation (Equation 1.9) can have more than one solution resulting in multiple images on the sky; if this happens the lens is said to be *strong*. This condition may be quantified using a dimension-less surface mass density, or *convergence*, κ:

$$\kappa(\boldsymbol{\theta}) = \frac{\Sigma(\boldsymbol{\xi})}{\Sigma_{\mathrm{crit}}} \tag{1.11}$$

where Σ_{crit} is the *critical surface mass density* which is defined as

$$\Sigma_{\mathrm{crit}} = \frac{c^2}{4\pi G} \frac{D_s}{D_l D_{ls}} \tag{1.12}$$

If the surface mass density is greater than this critical limit, i.e. if $\kappa \geq 1$, then multiple images are produced and we enter the strong lensing regime. The convergence may also be integrated over to define the *lensing potential* ψ of the system:

$$\psi(\boldsymbol{\theta}) = \frac{1}{\pi} \int_{\mathbb{R}^2} \kappa(\boldsymbol{\theta}') \ln |\boldsymbol{\theta} - \boldsymbol{\theta}'|\, \mathrm{d}^2\theta' \tag{1.13}$$

which can be related to the reduced deflection angle via $\boldsymbol{\alpha} = \nabla\psi$; the deflection angle is thus the gradient of the deflection potential. It also satisfies Poission's equation $\nabla^2\psi(\boldsymbol{\theta}) = 2\kappa(\boldsymbol{\theta})$.

Having introduced the basic concepts in gravitational lensing theory, I now move on to observational applications. Though the main emphasis of this Thesis is *weak lensing* it is instructive to briefly touch upon the related topics of *microlensing* and *strong lensing* as well.

1.2.2 Microlensing

In the beginning of last century, Einstein's theory of General Relativity (GR) was still new and required observational evidence for credibility. Gravitational microlensing provided such early evidence when Eddington set out on an expedition to confirm Einstein's prediction that a star passing close to the Sun would appear displaced due to its gravitational field. The exact displacement predicted by GR was 1.75 arcsec for a star at the solar limb, whereas Newtonian gravity predicted a mere 0.87 arcsec (i.e. half that of GR). To discriminate between the two theories, Eddington took advantage of the full solar eclipse on May 29, 1919. The displacement found by him and his collaborators was 1.61 ± 0.30 arcsec which clearly favours General Relativity (Dyson et al., 1920) and shows the power of the gravitational lensing technique.

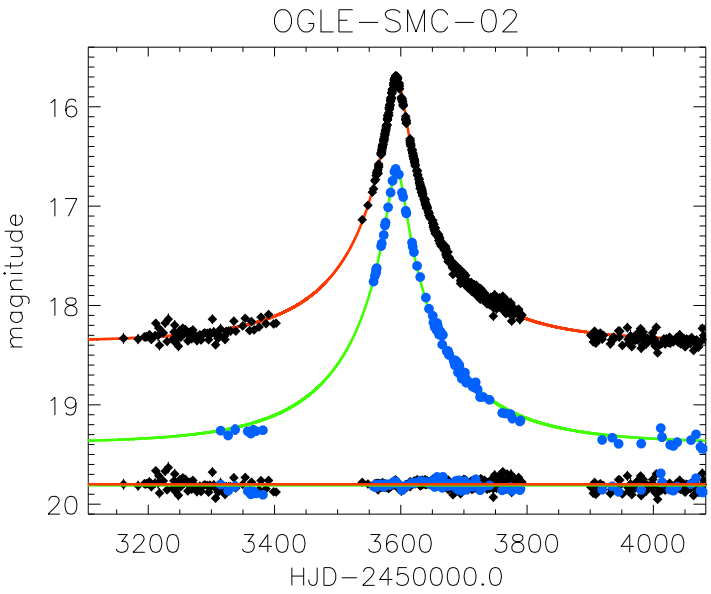

Figure 1.6 Example lightcurve caused by a microlensing event. The top two datasets are the same event observed in different filters, with the best-fit microlensing model shown as well. The bottom graph shows the residuals of the model fit. Figure originally published in Wyrzykowski et al. (2011).

Microlensing is a transient effect, caused by a foreground object often located in our own Milky Way galaxy passing in front of a bright background source. As the alignment between the source, the lens and the observer changes, the apparent brightness of the source is boosted and then diminished, causing the characteristic shape of the light curve shown in Figure 1.6. Since the event is transient, a potential source has to be monitored for some time to observe an event, but unfortunately such an event cannot be predicted. The probability of microlensing being observed is thus very low and therefore large dedicated surveys regularly scanning millions of stars are crucial for detection. Generally these surveys are trained towards areas with a high density of background stars, such as the centre of the Galaxy or another nearby galaxy like the Large Magellanic Cloud (LMC) or Andromeda. The microlensing *optical depth* is a measure of the probability of a source undergoing a microlensing event at a given time; the optical depth towards the centre of our Galaxy is $\tau = 2.43 \times 10^{-6}$ (Alcock et al., 2000b) while the equivalent measure towards the LMC is $\tau = 3.6 \times 10^{-8}$ (Tisserand et al., 2007). However, choosing a suitable backdrop is more dependent on which type of population is to be observed. If we are interested in objects in the halo of our Galaxy for instance, the galactic bulge is unavailable to us and an external galaxy is necessary.

Currently there are two major applications of microlensing: the search for MACHOs and other dark transient objects, and the search for extrasolar planets. A MACHO passing in front of a star would produce a light curve such as the one shown in Figure 1.6 but the lensing object itself would not be seen.

Therefore other potential causes of a change in brightness, such as the intrinsic variability of the source star, have to be ruled out before a successful detection can be claimed. Two collaborations that have been working to identify candidates in the Milky Way halo are the MACHO and EROS collaborations. MACHO's results contradict the hypothesis that our halo consists of MACHOs, effectively ruling out the theory that dark matter is composed of such massive objects (Alcock et al., 2000a). EROS provided agreement with these findings; they found that the maximum fraction of the halo mass that could consist of MACHOs is 8% (Tisserand et al., 2007). They also ruled out MACHOs in the mass range $0.6 \times 10^{-7}\ M_\odot < M < 15\ M_\odot$ as the primary occupants of the halo.

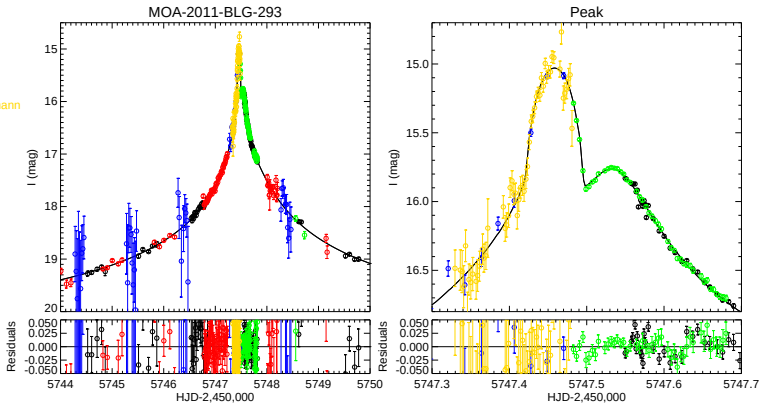

Figure 1.7 Example lightcurve caused by the star-and-planet system MOA-2011-BLG-293. The top two panels show the full light curve (left) and an enlarged view of the peak (right), with the best-fit microlensing model also shown in each case. The bottom panels show the residuals of each model fit. Figure originally published in Yee et al. (2012).

If the lens consists of more than one object, such as a binary star or a star and a planet, the light curve displays several peaks as illustrated in Figure 1.7. This is a direct way of finding extrasolar planets and determining their properties. From the observed light curve alone, the mass distribution in the lens may be deduced and thus the mass of the planet(s) can be determined. To date, 15 extrasolar planetary systems, with planets ranging in mass from 0.01 M_J to 3.7 M_J and separations of 0.66 AU to 5.1 AU, have been discovered using this technique (Yee et al., 2012; Bennett et al., 2012). This number is relatively low compared to the rival radial velocity detection method, but the list is rapidly growing as surveys collect more data. Such surveys include the Optical Gravitational Lensing Experiment (OGLE: Udalski et al., 1992; Udalski, 2003) and Microlensing Observations in Astrophysics (MOA: Bond et al., 2001; Sumi et al., 2003). An interesting discovery to come out of MOA is that of a population of planetary-mass objects that are seemingly not gravitationally bound to host stars (Sumi et al., 2011). Such a population could be explained via various scattering scenarios, but the number of candidate planets found indicates that the size of the population is almost twice that of main-sequence stars. This is larger than would be expected from scattering. However, the planets are only defined as isolated because no corresponding star was detected during the mi-

crolensing event. Sumi et al. (2011) offered the explanation that the planets may simply be bound in a very large orbit which gives a lower bound on their separation of $7 - 45$ AU. None the less, this discovery could have an impact on planet formation theories if the planetary objects are indeed orphaned (Bowler et al., 2011). The power of microlensing thus lies with its ability to detect dark compact objects in our own Galaxy and those nearby, thereby challenging theories of both dark matter and thus cosmology, and of planet and star formation. For applications of the related theories of strong and weak lensing, however, we have to move to a much grander scale.

1.2.3 Strong lensing

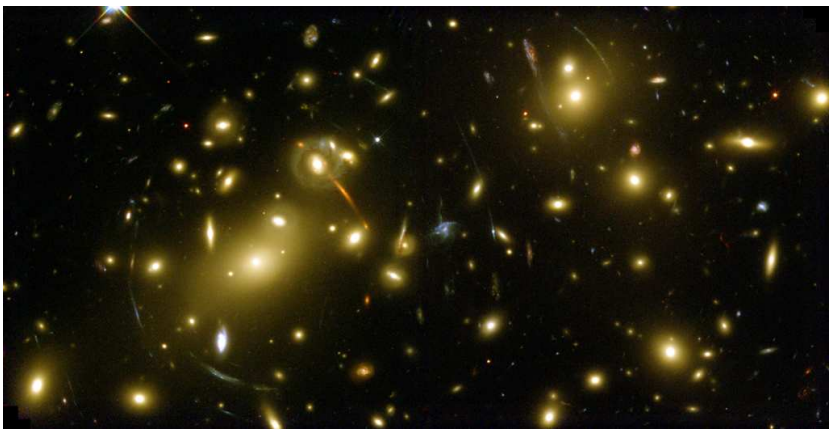

Figure 1.8 Example of strong lensing: the massive galaxy cluster Abell 2218 imaged by the Hubble Space Telescope in 1999. Image credit: NASA/ESA, A. Fruchter and the ERO Team (STScI, ST-ECF).

Distant clusters of galaxies display remarkable arc-like images such as those manifested in the stunning Abell 2218 (Figure 1.8). These source images are clear examples of strong gravitational lensing and typically appear in massive structures such as galaxy clusters or close to individual galaxies. As mentioned in the introductory Section 1.2.1, a condition for strong lensing is that the surface density is greater than the critical limit $\Sigma_{\rm crit}$, i.e. that $\kappa \geq 1$. Alternatively, for a source which is much smaller than the angular scale on which lens properties change, the mapping between source and lens plane can be linearised using a Jacobian matrix $\mathbf{A}(\boldsymbol{\theta})$:

$$f(\boldsymbol{\theta}) = f^s \left[\boldsymbol{\beta}_0 + \mathbf{A}(\boldsymbol{\theta}_0) \cdot (\boldsymbol{\theta} - \boldsymbol{\theta}_0)\right] \tag{1.14}$$

where f is the observed surface brightness distribution in the lens plane, f^s is the corresponding brightness distribution in the source plane, $\boldsymbol{\theta}_0$ is a point within the image corresponding to the point $\boldsymbol{\beta}_0$ within the source and

$$A_{ij}(\boldsymbol{\theta}) \equiv \frac{\partial \beta_i}{\partial \theta_j} = \delta_{ij} - \partial_i \partial_j \psi(\theta) \tag{1.15}$$

where we use the shorthand $\partial_i \equiv \partial / \partial \theta_i$. The *magnification* μ is the ratio of the observed flux from the image to that from the unlensed source, and this is

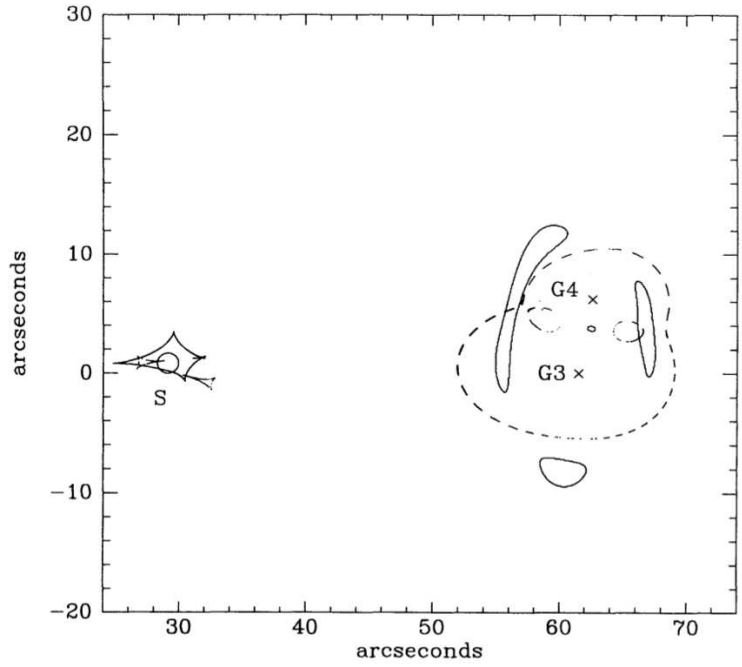

Figure 1.9 Strong lensing reconstruction of (part of) Abell 2218, with the cluster centre located at the origin. The crosses mark the two galaxies responsible for the majority of the lensing effect, and the arcs being modelled are also shown. The circle labelled S represents the size and location of the source. Dashed lines represent critical lines in the lens plane, while the curves close to the source represent the corresponding caustics. Figure originally published in Saraniti et al. (1996).

simply given by

$$\mu = \frac{1}{\det \mathbf{A}} \tag{1.16}$$

A more rigorous definition of strong lensing is then a system for which $\det \mathbf{A} = 0$, and in which multiple images are produced. A strong lens will have a locus in the image plane for which this condition holds true, and this locus is known as a *critical curve*. This curve can be visualised as a smooth loop. When the critical curve is mapped back to the source plane it is instead known as a *caustic* which will, contrary to its corresponding critical curve, generally display cusps. Along a critical curve, the magnification formally diverges and sources near these are highly magnified and distorted, resulting in the long arcs visible in Figure 1.8. The number of images associated with a particular source also depends on its vicinity to a critical curve, providing additional constraints. These effects are illustrated in Figure 1.9 which shows the reconstruction of a sub-cluster within Abell 2218, as modelled by Saraniti et al. (1996).

The main advantages of studying galaxy cluster lenses were recognised very early on by the bold visionary Zwicky who anticipated that we would be able to use clusters to trace the unseen mass (Zwicky, 1937), also predicted by himself (Zwicky, 1933). He further envisioned that given good enough imaging we

could study the distant sources behind clusters. Both these predictions have proved accurate, even though strong lensing was not observed until much later (e.g. the double quasar Q0957+561 and giant arcs; Walsh et al., 1979; Lynds & Petrosian, 1986; Soucail et al., 1987). Observers can use the arcs and multiple images in clusters or around single galaxies to model the critical curves and thus constrain the mass distribution within the lens. Lensing therefore offers a unique way to probe substructure. Clusters consist of several galaxies that are interacting now, or has done at some point in the past. Through these interactions and via their traversing through the cluster core, the extended dark matter haloes surrounding member galaxies are expected to be tidally stripped. This view is corroborated by evidence that cluster galaxies undergo strong morphological evolution including quenched star formation (e.g. Jones et al., 2000; Kodama & Bower, 2001; Treu et al., 2003). By accurately modelling the distribution of mass in the inner regions of clusters using individual cluster members, direct evidence of such stripping can be gathered, providing support for the theory of hierarchical merging as the main process in cluster assembly. The accuracy of such analyses is further improved by including weak lensing signals (see Section 1.3) since strongly lensed arcs are rare (e.g. Natarajan et al., 2007, 2009). Strong lensing has also been used to tentatively detect substructure in galaxy-size lenses consistent with predictions from ΛCDM (Vegetti et al., 2010).

As already mentioned, another use for these massive lenses is to employ them as Nature's own telescopes. Due to the great magnification effects involved we are privy to objects that would otherwise be too far away or too faint for us to see. These background objects do most likely not suffer from any prominent selection bias other than that related to the distances involved in the geometrical setup, although intrinsically brighter sources will produce brighter arcs for a given geometry. Though rare, magnifications of up to 4 magnitudes have been measured (Seitz et al., 1998) and increases in brightness of more than 1.5 magnitudes are relatively common (e.g. Richard et al., 2011). The magnification is wavelength independent, so the background sources can be fully studied for morphology and physical properties that would otherwise not be resolved. This yields insight into a very high redshift regime which we could not study in such detail directly. The *cosmic telescope* as a tool to detect high-redshift galaxies has since its first use heralded the discoveries of the most distant galaxies of their time (e.g. Franx et al., 1997; Ellis et al., 2001; Hu et al., 2002; Kneib et al., 2004). Some studies have claimed detections of candidate galaxies at redshifts as high as $z = 10.2$ using this technique (Stark et al., 2007), clearly on par with the highest-redshift galaxy candidate ever discovered ($z = 10.3$; Bouwens et al., 2011). Detecting and analysing such early galaxies is essential for our understanding of the era when the first stars and galaxies were assembled and objects such as quasars formed. It also provides vital clues to the process that led to the cosmic reionization, a crucial phase during the evolution of the early Universe.

Finally, strong lensing clusters have the power to constrain cosmology directly since the effect is dependent on angular diameter distances. These distances in turn are defined by the geometry of the Universe and in particular on the parameters Ω_m and w. For clusters with several arc sets due to sources at known but different redshifts, the Einstein radii may be compared. The ratio of the radii then holds information on the fundamental geometry of the Universe

(e.g. Link & Pierce, 1998; Golse et al., 2002; Soucail et al., 2004; Jullo et al., 2010). Encoded in arc properties is also the value of the Hubble parameter H_0. It can be constrained independently of cosmology by measuring the time delay between arcs originating from the same time-varying source (e.g. Blandford & Narayan, 1986; Saha et al., 2006; Oguri, 2007; Paraficz & Hjorth, 2010; Riehm et al., 2011). The number of giant arcs observed is also tied to the background cosmology, and in particular to the σ_8 parameter. Bartelmann et al. (1998) showed that the observed arc statistics differs from that predicted by ΛCDM, and this discrepancy has yet to be fully resolved. It may be explained by observational effects such as a poorly understood source population or substructure (Horesh et al., 2005), or physical effects due to baryons like cooling and star formation (Meneghetti et al., 2010). Furthermore, the observed giant-arc statistics may be an interesting indicator of primordial non-Gaussianity (D'Aloisio & Natarajan, 2011). Whatever the origin of the excess, it is clear that strong lensing has a lot to offer when it comes to confirming our understanding of cosmology. The applications of this effect are naturally focussed on large structures and although we have given only a brief overview here, clusters are very powerful probes of the geometry of the Universe (see Kneib & Natarajan, 2011, for a recent review). To take full advantage of these cosmological behemoths, however, we have to break away from the restrictions of strong lensing. Arcs are rare and contingent on serendipitous alignments and high-density regions. Combining the strengths of this technique with weak lensing, which is ubiquitous, will allow us to study clusters in ever more detail.

1.3 Weak lensing

Weak gravitational lensing is a relatively new study, with the first detection recorded by Tyson et al. (1990). Given sufficient depth and area, and good enough image quality, this statistical alignment of galaxies can be observed anywhere on the sky. The power of this technique to explore the unseen matter in clusters, in galaxies and even in the Cosmic Web is hence unrivalled. We will therefore review the fundamentals of this method in a bit more detail than its sister practices above, though for a thorough treatment we refer the reader to Bartelmann & Schneider (2001) and Schneider (2005).

1.3.1 Convergence, shear and flexion

As described in Section 1.2.1, a distinguishing limit between strong and weak lensing is the critical surface density $\Sigma_{\rm crit}$ and the related convergence κ. Starting from Equation 1.15 we can write the mapping between source and lens plane as

$$\beta_i \simeq A_{ij}\theta_j \tag{1.17}$$

This holds true for small source galaxies where the convergence is constant across the source image. Rewriting Equation 1.15 we can also get an alternative description of the distortion matrix $\mathbf{A}$:

$$\mathbf{A} = \begin{pmatrix} 1-\kappa-\gamma_1 & -\gamma_2 \\ -\gamma_2 & 1-\kappa+\gamma_1 \end{pmatrix} \tag{1.18}$$

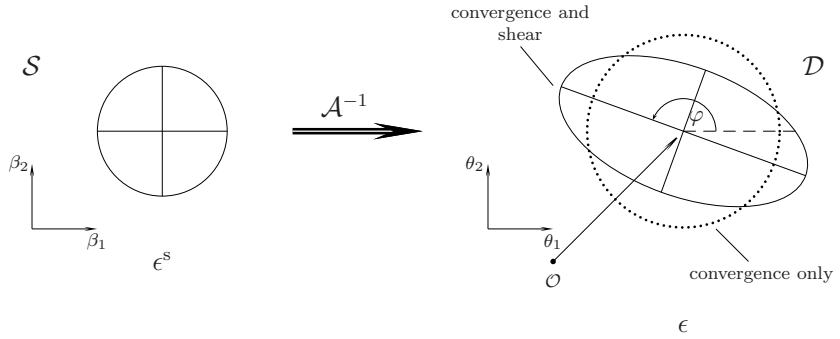

Figure 1.10 Effect of shear and convergence. On the left is the original circular source, while the lensed image is on the right. Convergence only results in an enlargement of the source image while the shear causes a stretch entailing a difference in axis ratio. The orientation of the resulting ellipse depends on the relative amplitudes of γ_1 and γ_2 as illustrated in Figure 1.11. This figure was originally published in Schneider (2005).

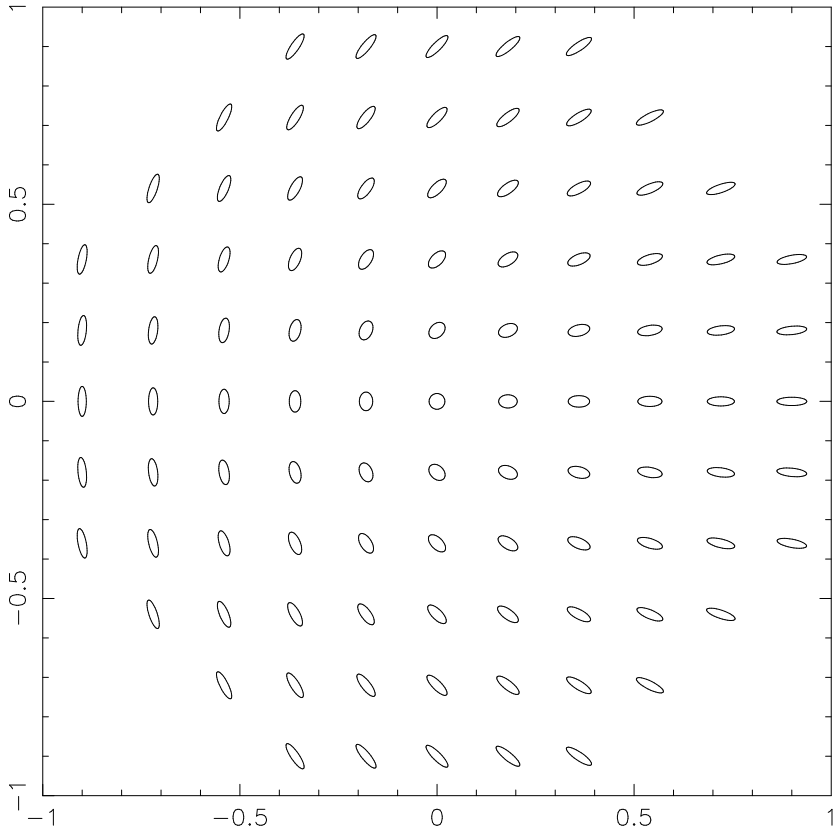

Figure 1.11 Orientation of the ellipse resulting from the relative amplitudes of γ_1 (on the x-axis) and γ_2 (on the y-axis) applied to a circular source. Figure originally published in Schneider (2005).

where γ_1 and γ_2 are the two components of the *shear* induced by the lensing potential: $\gamma = \gamma_1 + i\gamma_2$. These shear components are related to the lensing potential ψ via

$$\gamma_1 = \frac{1}{2}(\psi_{11} - \psi_{22}) \tag{1.19}$$

$$\gamma_2 = \psi_{12} \tag{1.20}$$

where e.g. $\psi_{11} = \partial_1^2\psi$ is the second derivative of the lensing potential. Defining the complex gradient operator

$$\partial = \partial_1 + i\partial_2 \tag{1.21}$$

using the same shorthand as before we can also relate the shear to convergence in a way which compactly shows that shear is the second-order gradient of the lensing potential:

$$\gamma = \partial\partial\psi \tag{1.22}$$

The effect of shear on a source image is to stretch it in one direction as illustrated in Figure 1.10 with the direction dependent on the relative amplitudes of the γ_1 and γ_2 distortions. As is clear from Figure 1.11, the transformation $\gamma \rightarrow -\gamma$ results in a 90° rotation and pure γ_2 is at 45° to pure γ_1. Generally we also assign a property known as *spin* to weak lensing distortions. A distortion type with spin s is invariant under a rotation of $\phi = 360°/s = 2\pi/s$ radians. Since an ellipse rotated by 180° looks the same, shear is a *spin-2 quantity*. The lensing displacement field α is a spin-1 quantity which is also the gradient of the spin-0 lensing potential:

$$\alpha = \alpha_1 + i\alpha_2 = \partial\psi \tag{1.23}$$

We can now interpret ∂ as a *spin-raising operator*; applying it once to the lensing potential results in a spin-1 quantity, while applying it twice results in spin-2. Similarly the complex conjugate ∂^* is a *spin-lowering operator*. For instance, the convergence is related to the lensing displacement field and lensing potential via

$$\kappa = \frac{1}{2}\partial^*\alpha = \frac{1}{2}\partial^*\partial\psi \tag{1.24}$$

and is thus a spin-0 quantity.

Equation 1.17 is an approximation that is sufficiently accurate when shear is constant across a source image. If this is is not the case, however, the equation has to be extended to higher orders to encapsulate the variations in shear:

$$\beta_i \simeq A_{ij}\theta_j + \frac{1}{2}D_{ijk}\theta_j\theta_k \tag{1.25}$$

where

$$D_{ijk} = \partial_k A_{ij} \tag{1.26}$$

is a third-order distortion tensor. The lensed surface brightness of a source may now be written

$$f(\boldsymbol{\theta}) \simeq \left\{1 + \left[(A - I)_{ij}\theta_j + \frac{1}{2}D_{ijk}\theta_j\theta_k\right]\partial_i\right\} f^s(\boldsymbol{\theta}) \tag{1.27}$$

where I is the identity matrix. The tensor D captures the distortions responsible for the arc-like shape of weakly lensed images, reminiscent of the giant arcs in

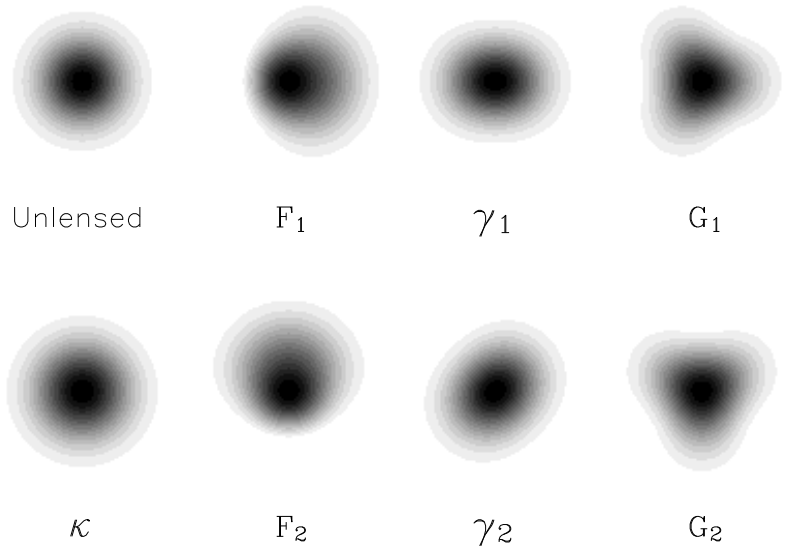

Figure 1.12 Illustration of convergence, shear and flexion distortions as applied to a circular source with a Gaussian density profile. The spin values, as described in the main text, increase from 0 for convergence to 3 for G flexion. Figure originally published in Bacon et al. (2006).

strong lensing (though the giant arcs are usually the result of several distorted images merging, unlike in weak lensing). This tensor can be succinctly expressed in terms of two new quantities, known as *flexion*:

$$D_{ijk} = \mathcal{F}_{ijk} + \mathcal{G}_{ijk} \tag{1.28}$$

where $\mathcal{F}$ is the first flexion, or *F flexion*, and $\mathcal{G}$ is the second flexion, or *G flexion*. The F flexion was first discovered and investigated a decade ago by Goldberg & Natarajan (2002) with a tentative detection in Goldberg & Bacon (2005). Bacon et al. (2006) then developed the notation further and included the G flexion as well. The flexions are the third-order derivatives of the lensing potential and the gradients of convergence and shear:

$$\mathcal{F} = \frac{1}{2}\partial\partial^*\partial\psi = \partial^*\gamma = \partial\kappa \tag{1.29}$$

$$\mathcal{G} = \frac{1}{2}\partial\partial\partial\psi = \partial\gamma \tag{1.30}$$

which, following the above discussion, means that F flexion is a spin-1 quantity while G flexion has spin-3. Convergence, shear and flexion are all illustrated in Figure 1.12.

It should be noted that, unlike convergence and shear, flexion is not dimensionless but has units of inverse length. Furthermore, throughout this Thesis we make the implicit assumption that we are working in the weak lensing regime, i.e. $\kappa \ll 1$. If this condition is broken, our observations would be biased since

what we truly observe are the quantities g, G_1 and G_3 (Schneider & Seitz, 1995; Schneider & Er, 2008):

$$g = \frac{\gamma}{1-\kappa} \tag{1.31}$$

$$G_1 = \partial^* g = \frac{\mathcal{F} + g\mathcal{F}^*}{1-\kappa} \tag{1.32}$$

$$G_3 = \partial g = \frac{\mathcal{G} + g\mathcal{F}}{1-\kappa} \tag{1.33}$$

where g is the *reduced shear* and G_1 and G_3 are the *reduced flexions*. This is a consequence of the *mass-sheet degeneracy*, a well-known potential source of bias in gravitational lensing. The degeneracy arises from the fact that the addition of a sheet of constant surface density in front of the lens will not alter the shear or flexion measurements (Falco et al., 1985). Breaking this degeneracy is possible with magnification measurements in principle, because the magnification reacts differently to a mass sheet. It has also been pointed out that there is some cross-talk between shear and flexion which has to be considered for an unbiased measurement (Viola et al., 2012). Both these effects are significantly reduced in impact in the weak lensing limit. Therefore I do not touch upon it further in this Thesis which is mainly concerned with the lensing signal induced by galaxy-sized halos, but use the approximation that the observed quantities are equivalent to the non-reduced quantities.

1.3.2 Cosmic shear

As light travels through space to reach us it is continuously deflected by the filaments and nodes of the Cosmic Web. Source galaxies are thus sheared and weakly aligned even when there are no large structures in the way. The statistics of these distortions and alignments therefore reflect the statistics of the underlying matter distribution. Though the distortion is minute at less than $\sim 1\%$, this effect was detected at the turn of the millennium (Bacon et al., 2000; Kaiser et al., 2000; Van Waerbeke et al., 2000; Wittman et al., 2000). It is since being measured with ever more refined accuracy using imaging data of ever increasing area, depth and quality, and used to constrain cosmological parameters (e.g. Hoekstra et al., 2002; Brown et al., 2003; Jarvis et al., 2003; Massey et al., 2005; Van Waerbeke et al., 2005; Hoekstra et al., 2006; Semboloni et al., 2006; Benjamin et al., 2007; Schrabback et al., 2007; Fu et al., 2008; Schrabback et al., 2010; Huff et al., 2011). The correlation between shears across the sky as a function of angular scale can be used to derive the lensing power spectrum which is related to the three-dimensional matter power spectrum (e.g. Kaiser, 1992; Bartelmann & Schneider, 2001; Schneider, 2005; Hoekstra & Jain, 2008). Technically, cosmic shear cannot make use of the thin lens approximation used to derive the lensing results quoted so far in this Introduction because the deflection does not take place in a single lens plane. It turns out, however, that under the assumption that the deflection angle is small the end result is a redshift-dependent convergence κ which behaves just like in ordinary lensing (see e.g. Schneider, 2005). We can therefore use ordinary shear measurements to constrain the matter power spectrum, and thus in particular the cosmological parameters Ω_m and σ_8.

Since the measurements do not rely on baryonic tracers there are no assumptions on e.g. galaxy bias necessary and this gives cosmic shear great value. Furthermore, the constraints resulting from cosmic shear intersect the constraints from the CMB in a way that reduces degeneracies adding to the benefits of such analyses. The task of observing this effect is a fairly substantial challenge however, owing to the fact that the distortions are so small. It is impossible to detect a signal on a single galaxy image since the intrinsic ellipticity of the source galaxy is in general much larger than the induced distortion. Assuming that galaxies have random intrinsic ellipticities and that they are randomly oriented on the sky we can discern the lensing signal in a statistical way though. If we average over enough sources we can reduce this *shape noise* and essentially reason that the mean intrinsic shape is circular. Under ideal conditions, any ellipticity observed must then be produced by lensing.

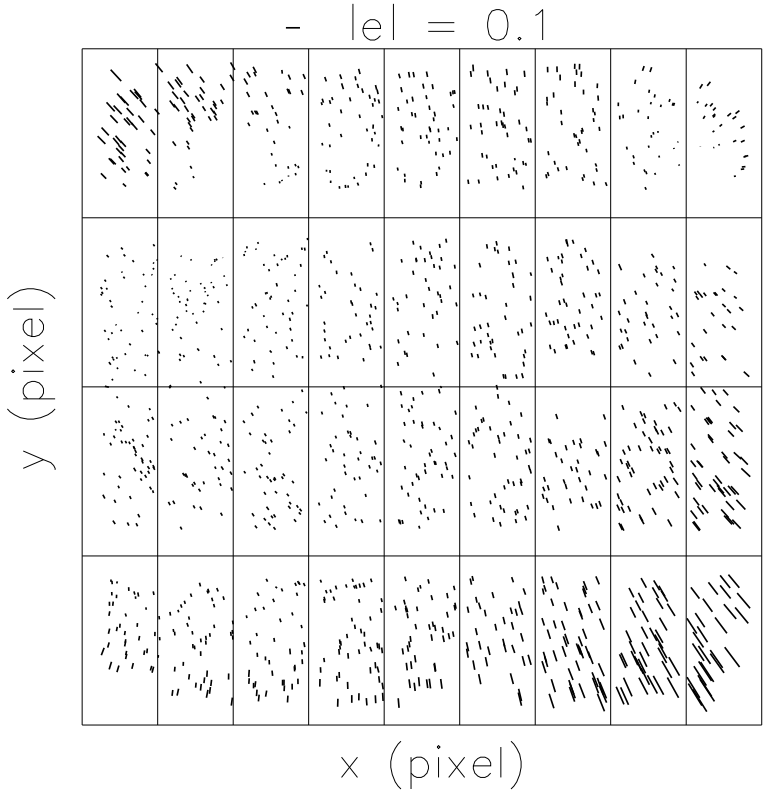

Figure 1.13 Point-spread function (PSF) pattern of a typical field in the Canada-France-Hawaii Telescope Legacy Survey (CFHTLS). Each tick represents the observed magnitude and orientation of a stellar ellipticity. The artificially induced ellipticity is most prominent in the corners in this case. Figure originally published in Fu et al. (2008).

Unfortunately, such ideal conditions are also difficult to attain. A telescope will in general produce a complicated pattern which correlates galaxy ellipticities in a way that imitates a lensing signal. This pattern, illustrated in Figure 1.13, is

usually referred to as the *point-spread function* (PSF), although other distinct processes can be involved as well (such as wind-shake of the telescope). For ground-based surveys the PSF is worsened by turbulence in the atmosphere and these *seeing* conditions tend to blur the galaxy images and dilute their ellipticities. Generally the PSF is corrected for by taking advantage of the fact that stars should be circular. Any ellipticity observed for stars is therefore due to the PSF and this information may be used to model the distortions. Space-based telescopes face other trials, however, such as the gradual degradation of CCD chips due to the constant bombardment of cosmic radiation (resulting in charge-transfer inefficiency or CTI; see e.g. Rhodes et al., 2007, 2010). CTI is the result of so-called charge traps in the silicon surface of a CCD which reveal themselves as artificial trails behind objects on an astronomical image. Again, this can cause a false shear detection if left unaccounted for. Recently though, promising ways to correct for this effect have been suggested either at an image reconstruction level (Massey et al., 2010) or parametrically (as in e.g. Schrabback et al., 2010).

Additional difficulties include the fact that detectors collect photons in square bins (or *pixels*) which places a fundamental lower limit on the size galaxy that can be reliably analysed, and the fact that there is some *intrinsic alignments* of galaxies due to them being affected by tidal fields during formation (e.g. Splinter et al., 1997; Faltenbacher et al., 2002; Lee & Pen, 2008) or lower-redshift tidal fields affecting all higher-redshift sources (Hirata & Seljak, 2004; Heymans et al., 2006b). Another limiting factor is the accuracy of the software used to extract the shear signal from a given image. Great effort has been put into developing reliable software and at the moment there are many alternatives available. To take full advantage of future surveys, however, the accuracy has to be improved even more. An overview of the current shape measurement software state-of-the-art is given in Section 1.3.5, but first I will introduce a different weak lensing application which is more robust against issues such as PSF and CTI: galaxy-galaxy lensing.

1.3.3 Galaxy-galaxy lensing

The source images due to a lens galaxy will be aligned in a circular pattern around the lens, and the distortions of the sources decrease in strength the further from the lens they are. By measuring the average lensing distortion in circular bins of successively increasing size centred on the lens, a function will emerge that encodes the *density profile* of the lens, i.e. it tells us how the mass is distributed within the lens. Since the distortions are weak in general, we again have to average over many lenses and sources in order to decrease the shape noise. This way we can study the density profiles of a galaxy population in a statistical fashion, a technique known as *galaxy-galaxy lensing*. Galaxy-galaxy lensing may also be applied to clusters to complement strong lensing (where available) and to map the matter distribution in these more complicated systems.

The shear components γ_1 and γ_2 and the equivalent flexion components are defined with respect to a Cartesian coordinate system. For galaxy-galaxy lensing studies it is more convenient to define components relative to the lens that the sources are centred on. It is therefore common practice to adopt *tangential* and

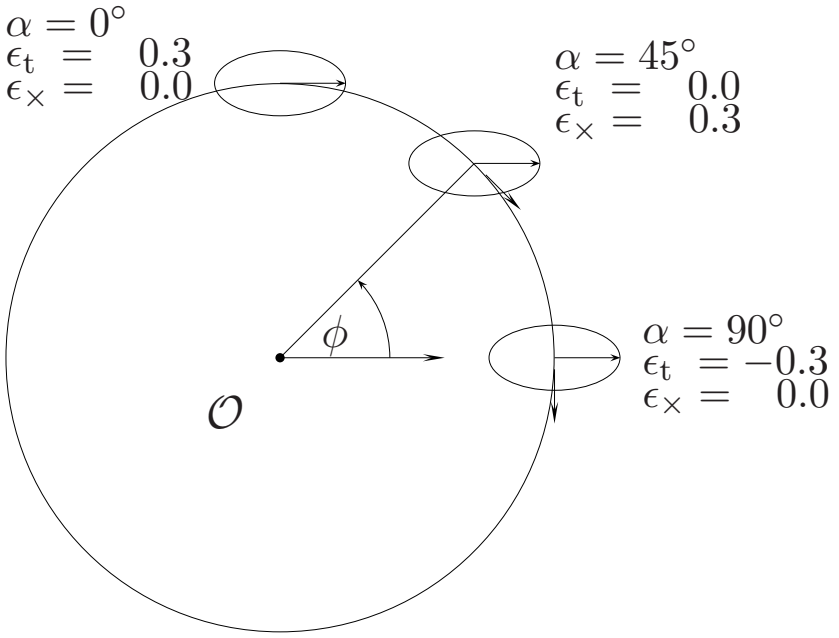

Figure 1.14 Illustration of the tangential and cross components of shear for a circular lens located at the origin $\mathcal{O}$. The background source is located at angle ϕ relative to the horizontal. For a tangentially aligned source, the tangential shear ϵ_t (γ_t in the text) is positive and the cross term $\epsilon_\times$ ($\gamma_\times$) is zero; if ϵ_t is negative instead then the source is radially aligned. A positive or negative cross term with no tangential component signifies a source image angled at 45° relative to the lens. Figure originally published in Schneider (2005).

cross components, γ_t and $\gamma_\times$:

$$\gamma_t = -\Re[\gamma e^{-2i\phi}] = -\cos(2\phi)\gamma_1 - \sin(2\phi)\gamma_2 \quad (1.34)$$
$$\gamma_\times = -\Im[\gamma e^{-2i\phi}] = \sin(2\phi)\gamma_1 - \cos(2\phi)\gamma_2 \quad (1.35)$$

where ϕ is the angle between lens and source image as illustrated in Figure 1.14. Similarly we can define the corresponding components for the flexions:

$$F_t = -\cos(\phi)\mathcal{F}_1 - \sin(\phi)\mathcal{F}_2 \quad (1.36)$$
$$F_\times = \sin(\phi)\mathcal{F}_1 - \cos(\phi)\mathcal{F}_2 \quad (1.37)$$
$$G_t = -\cos(3\phi)\mathcal{G}_1 - \sin(3\phi)\mathcal{G}_2 \quad (1.38)$$
$$G_\times = \sin(3\phi)\mathcal{G}_1 - \cos(3\phi)\mathcal{G}_2 \quad (1.39)$$

where the effect of the spin property is clear in the multiplication factor of the angle ϕ. Averaging as described above, a lensing mass would produce a purely positive tangential signal while a so-called *void* (underdensity) would cause a purely negative signal. The cross terms can never be induced by lensing (for an isolated circular lens) and measurement of such a signal therefore provides a good null test for systematic errors (or *systematics* for short).

Since sources are averaged in circles relative to lens positions, galaxy-galaxy lensing is less sensitive to systematics such as PSF or CTI which tend to induce

correlation between shapes across an entire observed field. There are however other systematics that have to be taken into account. The main concerns include intrinsic alignments of satellite galaxies (see Section 1.3.2) diluting the signal, and neighbouring galaxies at the same redshift having a similar effect simply because they are not lensed. By using redshift information for both lenses and sources these effects can be minimised however, illustrating the importance of accurate redshift measurements for weak lensing analyses. Since weak lensing surveys are generally very large and there are millions of galaxies involved, spectroscopic redshifts are unfeasible. Fortunately, state-of-the-art photometric redshift software is able to produce reliable redshift estimates (see e.g. Hildebrandt et al., 2012, for recent CFHTLS results). Additionally, as suggested by Rowe (2008) and further investigated in Velander et al. (2011) (Chapter 3 in this Thesis), the light from lens galaxies may be bright enough to affect the source shapes measured, particularly in the case of F flexion. This effect can be avoided by not using sources too close to other bright light sources such as the lens. The amplitude of the flexion signal falls off very quickly with distance, however, and we therefore have to go close to the lens in order to detect it. An alternative approach is to model the lens light and remove it from the image before measuring the source shapes (see Section 3.4.3, page 73). Though this seems to work well, we have to be careful not to introduce new artifacts.

Observing the density profiles of galaxies tells us about the total mass of the lenses which provides constraints on various relations between halo mass and the properties of the observed galaxy (see Chapter 4). It is also of interest because N-body simulations predict specific profiles. Confirming or disproving these profiles will provide clues to the underlying physics used when creating the simulation. There are currently two main density profiles being used in weak lensing to determine mass: the *singular isothermal sphere* (SIS) and the *Navarro-Frenk-White profile* (NFW; Navarro, Frenk, & White, 1996). The SIS is a fairly simplistic powerlaw for which the density is inversely proportional to the square of the physical radius r, $\rho(r) \propto r^{-2}$. For such a density profile the shear and flexion profiles are given by

$$|\gamma_t(\theta)| = \frac{\theta_E}{2\theta} \tag{1.40}$$

$$|F_t(\theta)| = \frac{\theta_E}{2\theta^2} \tag{1.41}$$

$$|G_t(\theta)| = \frac{3\theta_E}{2\theta^2} \tag{1.42}$$

where $\theta = \xi/D_l$ is the angular distance from the lens and θ_E is the Einstein radius:

$$\theta_E = 4\pi \left(\frac{\sigma_v}{c}\right)^2 \frac{D_{ls}}{D_s} \tag{1.43}$$

with σ_v the velocity dispersion of the lens. The velocity dispersion of a halo is directly related to its mass via

$$\sigma_v^2 = \frac{GM(r)}{2r} = \frac{1}{2} v_{\rm rot}^2 \tag{1.44}$$

where $M(r)$ is the mass interior to r and $v_{\rm rot}$ is the rotational velocity. This profile thus reproduces the flat rotation curves discussed in Section 1.1.2 since

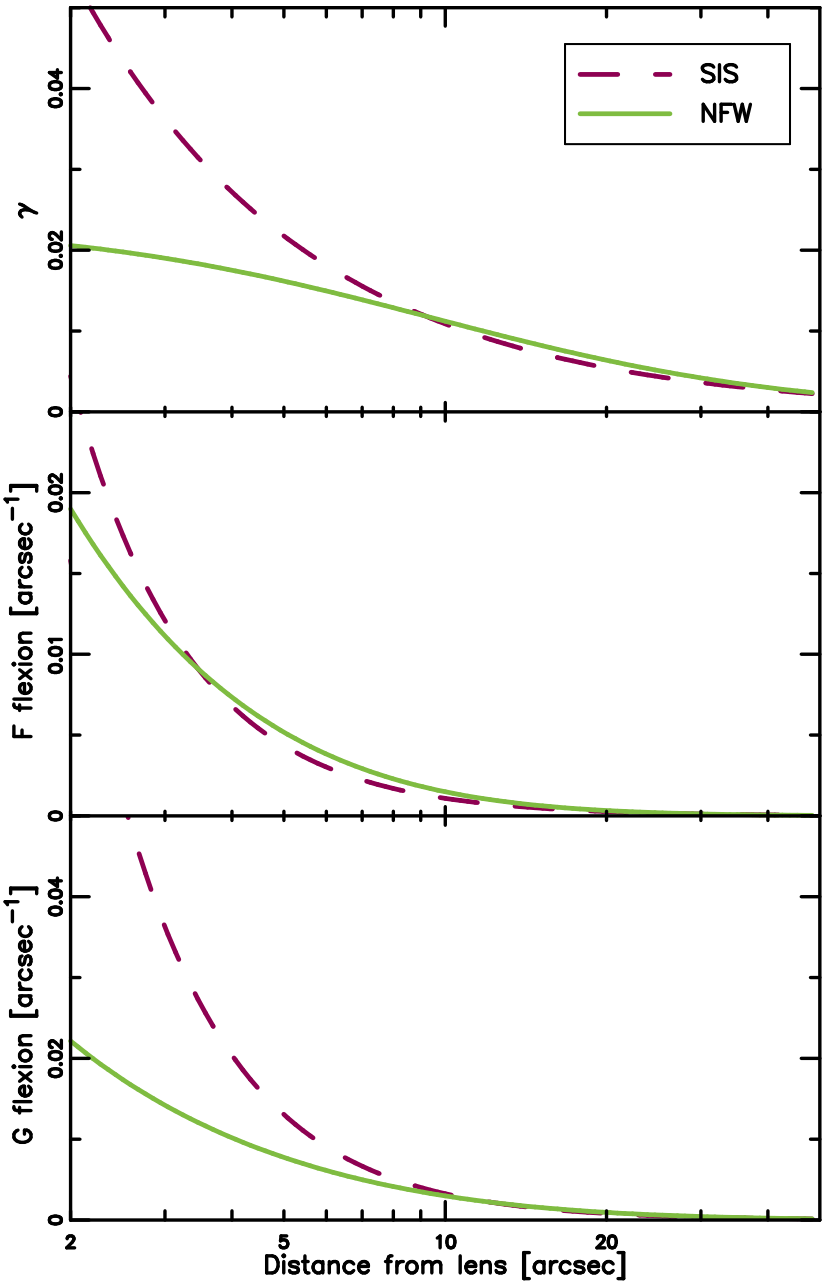

Figure 1.15 Comparison of the singular isothermal sphere (SIS) and Navarro-Frenk-White (NFW) density profiles for shear, F flexion and G flexion (top to bottom). The dashed (solid) line represents the SIS (NFW) profile in each case, and the surface mass density is proportional to the shear.

the rotational velocity is constant, but it is clearly unphysical close to the lens where the density profile approaches infinity.

The NFW profile is motivated by the properties of pure dark matter haloes in

N-body simulations and has a softer inner profile but approaches the behaviour of the SIS on larger scales. The density scales as

$$\rho(x) = \frac{\rho_{\rm crit}(z)\Delta_c}{x(1+x)^2} \tag{1.45}$$

where $x = r/r_s$ is the radius in units of a scaling radius r_s and Δ_c is a dimensionless scaling density. The shear profile for the NFW has been analytically derived by Wright & Brainerd (2000) and the corresponding flexion expressions are given in Bacon et al. (2006). A defining parameter of the NFW halo is also its *concentration* c which is related to its *virial radius* r_{200} within which the total mass is M_{200} (see e.g. Duffy et al., 2008, for a recent relation). The virial radius defines the point where the density of the halo is 200 times the critical density $\rho_{\rm crit}$. M_{200} is frequently used as a measure of the halo mass in weak lensing analyses, and a relation between the NFW halo mass and the SIS Einstein radius is given by e.g. Bacon et al. (2006). A comparison of the SIS and NFW profiles for each of shear, F flexion and G flexion is shown in Figure 1.15 for a halo of mass $M = 1 \times 10^{12}\ h^{-1}\ M_\odot$ at redshift $z_l = 0.35$. The lensing distortions shown are imprinted on sources at redshift $z_s = 0.8$. It is clear that the inner regions are important for distinguishing density profiles and this is an interesting application of flexion since it has the potential to better distinguish between the two profiles. In Chapter 3 we use space-based data to observe galaxy-galaxy flexion and use the measurements to constrain the density profile of an average galaxy.

These profiles are useful for studying isolated galaxies or for characterising the mass distribution on small scales, close to the lens. However, we know that galaxies in general cluster along dark matter filaments and in Cosmic Web nodes. If we do not specifically select galaxies that are isolated, we will see an excess signal on larger scales due to neighbouring galaxies and their haloes adding their signature to the profile. To extract an accurate mass estimate this fact has to be accounted for, and the established approach is to use a *halo model* (e.g. Cooray & Sheth, 2002; Guzik & Seljak, 2002; Mandelbaum et al., 2005; van Uitert et al., 2011). The model becomes more complicated when the lensing signal contribution from satellite galaxies is also included, and when striving to accurately account for the normal baryonic matter in galaxies as well, rather than just the dark matter. In Chapter 4 we briefly review the halo model introduced in van Uitert et al. (2011) and apply it to data from the full Canada-France-Hawaii Telescope Legacy Survey (CFHTLS) with the aim of learning about the connection between dark matter haloes and their corresponding host galaxies. For genuine galaxy clusters however, the approach is slightly different. We discuss this in more detail in Chapter 5, but first I give a qualitative example of the impressive cluster results that can be achieved with weak lensing.

1.3.4 Bullets and train wrecks

The power of combining a weak lensing analysis with other types of mass observations is well illustrated by recent studies of merging galaxy clusters. The merging process causes the matter distribution in such clusters to be highly disturbed, allowing us to study the behaviour of their mass components under such unusual circumstances. This Section will mainly be concerned with two

such clusters which are in stark contrast to each other: the Bullet Cluster (1E 0657-558) at $z = 0.296$ and the Cosmic Train Wreck (Abell 520) at $z = 0.201$.

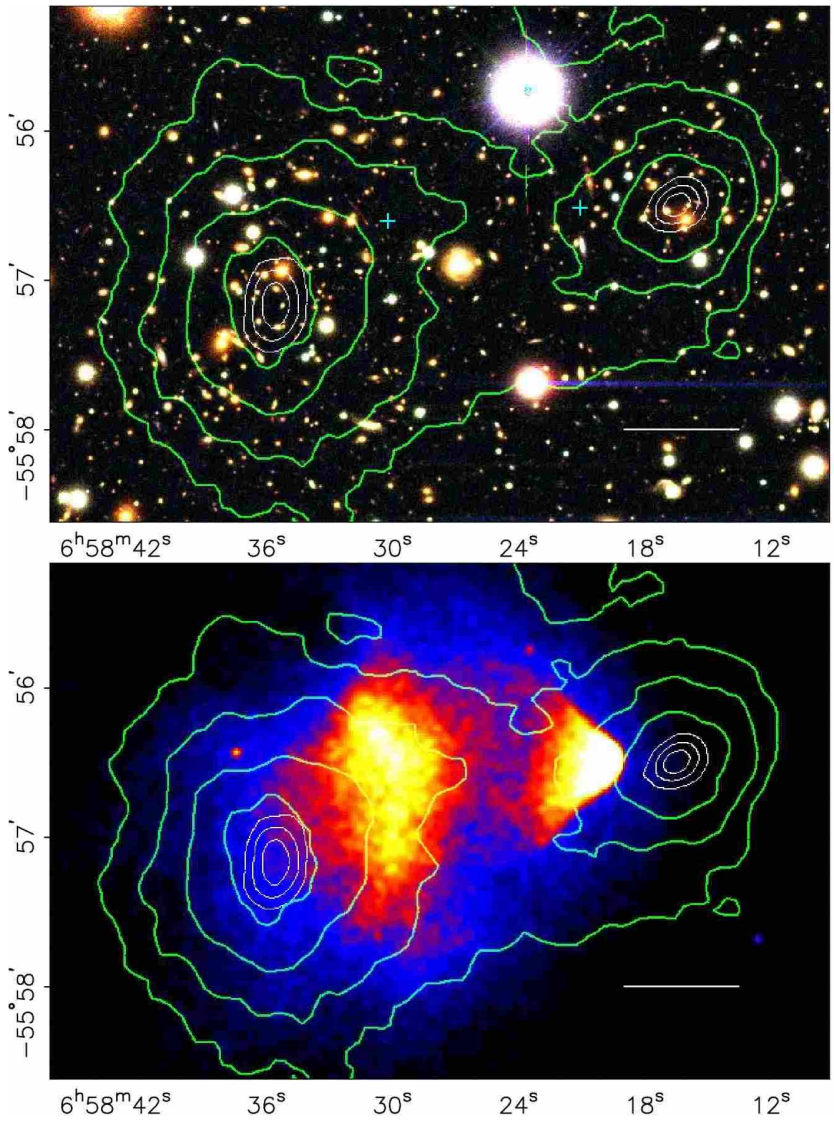

Figure 1.16 Bullet Cluster weak lensing results. The top panel shows the galaxies imaged with the Hubble Space Telescope and the bottom panel shows the plasma imaged with Chandra. Overlaid on both panels are the green contours from the weak lensing analysis, the peaks of which clearly coincide with the two galaxy concentrations rather than with the plasma concentration which contains more baryonic mass. Figures originally published in Clowe et al. (2006).

The Bullet Cluster was made famous by Clowe et al. (2006) when they presented a study where a weak lensing mass reconstruction is compared to the locations of baryons in the cluster. The baryonic components considered in that paper are the galaxies themselves in each of the two merged clusters, and the

plasma displaced from the clusters during the collision. Their results are shown in Figure 1.16 and they are in excellent agreement with what ΛCDM predicts. As the two main clusters pass through each other the galaxies act essentially as collisionless particles and emerge on either side relatively intact. The plasma from each cluster on the other hand is caught in the middle as evidenced by the 'bullet' or shock wave visible in the X-ray imaging (lower panel in Figure 1.16). In the absence of dark matter we would expect the majority of the mass to be contained in the plasma. As is clear from the weak lensing analysis, shown as green contours in Figure 1.16, the mass peaks coincide perfectly with the two galaxy concentrations and there is no evidence of a peak near the bullet. This is consistent with the prediction that dark matter is collisionless and should thus follow the galaxies as the two clusters pass through each other. Since the observations are difficult to explain with models that just modify the gravity strength of ordinary matter, this particular study has become a standard piece of evidence for the existence of dark matter.

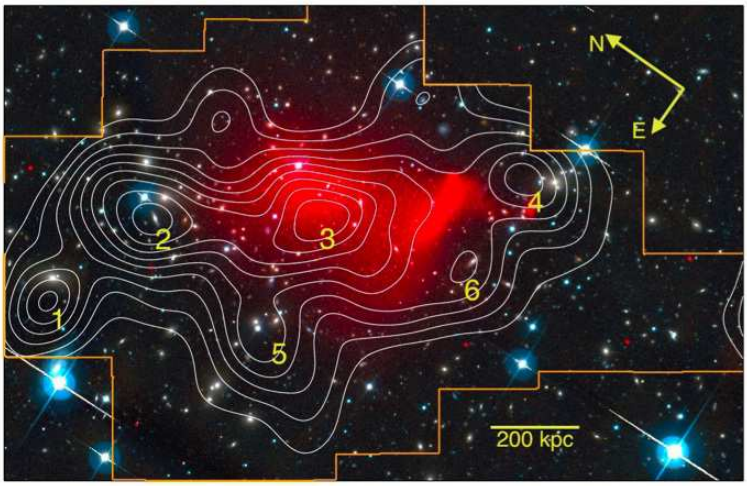

Figure 1.17 Cosmic Train Wreck weak lensing results. The weak lensing mass contours are overlaid a composite image showing both the optical CFHT observations and the Chandra X-ray observations as a diffuse red cloud. Significant weak lensing mass peaks are numbered 1-6 and number 3 coincides with a high plasma concentration in this case, contrary to what is seen in the Bullet Cluster. Figure originally published in Jee et al. (2012).

As a counter-example, the Cosmic Train Wreck which is a merging cluster thought to be at a stage similar to that of the Bullet Cluster has been studied using the same approach (Mahdavi et al., 2007; Jee et al., 2012). The resulting composite image (Figure 1.17) shows six distinct weak lensing mass peaks. Most of these peaks coincide with concentrations of galaxies, with the glaring exception of peak number 3. There are a few faint cluster galaxies in the vicinity of this peak but, more strikingly, that area seems dominated by the high plasma density. This is very puzzling because it seems to indicate that there is

dark matter, *but no associated luminous matter*, left at the centre of the cluster suggesting that the dark matter particles have collided. Comparing the dark matter collisional cross-section estimated from this analysis with the maximum allowed value derived from the Bullet Cluster, it becomes clear that the two analyses are incompatible at a 6σ level. There have been a few suggested explanations for this result, including a Cosmic Web filament centred on peak 3 and pointing straight towards or away from us, but there have to be a fair few fortuitous circumstances for any of these explanations to hold. If all other explanations are ruled out and we are left with collisional dark matter as the only possibility, then the Cosmic Train Wreck constitutes a strong counter-argument to the conclusions drawn from the Bullet Cluster.

These two examples showcase the ability of weak lensing to reveal basic properties of dark matter, thanks to its sensitivity to *all* matter structure in the foreground. It also shows the scientific value in analysing not only well-behaved large structures with settled features but also atypical cases with heavily distorted mass distributions. It is clear that there is a great deal to be learnt via analyses like these.

1.3.5 Shape measurement methods

The challenge of correctly determining the lensing distortions is a significant one. As already discussed, the distortions are small and imprinted on galaxies which are not intrinsically circular. Furthermore, our view of the resulting source images is somewhat muddled by the imaging systems we use to observe them and, in the case of ground-based telescopes, by the atmosphere. Considerable effort has gone into producing a method that can reliably measure shear and flexion, though most of the effort has so far been focused on recovering the shear only. As a result there is a wide variety of shape measurement methods in use today, and I will here give an overview of the most common types.

Moments-based methods

A widespread approach to determining the shape of a galaxy image is to measure the *moments* of its surface brightness distribution. The first (or monopole) moments $\bar{x}$ and $\bar{y}$ correspond to the *centroid* while the second (or quadrupole) moments Q_{ij} encode the ellipticity and higher order (octupole and 16-pole) moments Q_{ijk} and Q_{ijkl} are related to the flexions. By combining these moments, estimators for shear and flexion may be derived in the weak lensing limit (see e.g. Okura et al., 2008):

$$\gamma \simeq \frac{1}{2}\langle\chi\rangle \tag{1.46}$$

$$\mathcal{F} \simeq \left\langle \frac{\zeta}{(9/4) - 3(\mathrm{tr}Q)^2/\xi} \right\rangle \tag{1.47}$$

$$\mathcal{G} \simeq \frac{4}{3}\langle\delta\rangle \tag{1.48}$$

where χ, ξ, ζ and δ are moments combinations:

$$\chi \equiv \frac{Q_{11} - Q_{22} + 2iQ_{12}}{Q_{11} + Q_{22}} \tag{1.49}$$

$$\xi \equiv Q_{1111} + 2Q_{1122} + Q_{2222} \tag{1.50}$$

$$\zeta \equiv \frac{Q_{111} + Q_{122} + i(Q_{112} + Q_{222})}{\xi} \tag{1.51}$$

$$\delta \equiv \frac{Q_{111} - 3Q_{122} + i(Q_{112} - Q_{222})}{\xi} \tag{1.52}$$

In most applications a weight function is applied to the moments in order to limit the effect of noise; these are then known as *weighted moments* and form the basis of the currently most common family of shape measurement methods — the Kaiser-Squires-Broadhurst method (KSB; initially suggested and subsequently developed by Kaiser, Squires, & Broadhurst, 1995; Luppino & Kaiser, 1997; Hoekstra, Franx, Kuijken, & Squires, 1998). A fundamental limitation of KSB is the simplifying assumptions it makes regarding the PSF which are not applicable to more realistic functions (Kaiser, 2000). Even so, the method has been highly successful in practice and the recovered shear still compares well with newer methods. KSB now comes in many flavours, most of them measuring shear only (e.g. Bacon et al., 2000; Erben et al., 2001; Heymans et al., 2005; Schrabback et al., 2007). The extension of KSB to higher orders and thus flexion is known as higher-order lensing image characteristics (HOLICs; Okura et al., 2007, 2008). Additionally, some methods keep to the general philosophy of KSB but vary the weight function (e.g. DEIMOS; Melchior et al., 2011).

Model-fitting methods

The PSF limitation in KSB has inspired the development of alternative methods, and many of them are based on characterising the galaxy brightness distribution through model-fitting. The variation between techniques here is greater than for the moments-based methods simply because there are many different ways to model a galaxy. The general idea is the same though: create a circular or elliptical model galaxy and compare it to an observed source image to determine how much it has been sheared by. The PSF can be accounted for either by convolving the model galaxy with the observed pattern or deconvolving the observed image, though the latter is often discarded due to the difficulty of performing such an operation and its detrimental effect on noise properties.

One way to compare the model galaxy to the source image is to decompose them both into a series of so-called *Shapelets* (Bernstein & Jarvis, 2002; Refregier, 2003; Refregier & Bacon, 2003). The advantage of doing so is to gain analytical expressions for PSF convolution, shear and flexion, making the calculations exact and fast. Shapelets also allow for a more realistic description of the PSF than the one utilised by KSB. This method, however, fundamentally assumes that galaxies are well described by a Gaussian brightness distribution and this limits the reach of the components. Therefore the wings of galaxies are often not well constrained unless very high orders are used, something which is usually difficult because of a lack of pixels. Never the less this approach has proven efficient and accurate and there are several implementations available (Kuijken, 2006; Massey et al., 2007b; Nakajima & Bernstein, 2007; Velander

et al., 2011). This Thesis recounts in part the development of the Velander et al. (2011) version and the use of it to detect flexion in space-based data (see Chapters 2 and 3). A related approach is that of Sérsiclets (Ngan et al., 2009; Andrae et al., 2011) which uses a more realistic basis set derived from the *Sérsic* description of galaxy brightness profiles (Sérsic, 1968). The galaxy can also be modelled as a sum of elliptical Gaussians (Kuijken, 1999; Bridle et al., 2002; Voigt & Bridle, 2010).

In general the above shape measurement pipelines use a least-squares fitting technique, or equivalent, to determine the relevant parameters of the brightness distribution. A different procedure is to use Bayesian statistics, taking the full posterior probability in ellipticity into account. This is exemplified by LENSFIT (Miller et al., 2007; Kitching et al., 2008), a shear measurement software suite which has shown great promise in recent years, both in simulations and on real data. The galaxy images are modelled individually using the sum of two Sérsic profiles to represent the bulge and disk and a full likelihood surface is produced. This likelihood is then used to estimate the shear of the galaxy. However, Bayesian model fitting requires a *prior* (i.e. a best guess) and is therefore sensitive to the exact choice of such a prior. In principle it can be found iteratively using the data at hand, but it is still not clear exactly how strongly a wrong choice would affect the outcome. These worries are relevant for most model-fitting techniques though, since the introduction of additional information is often required due to models being under-constrained by the data. Another fundamental concern is that which also applies to all model-based methods: the model used to imitate a galaxy may not accurately represent the morphology of the true galaxy. To assess the impact of the choices and approximations made in any shear measurement method (be it moments- or model-based), it is vital to use simulated data where we know what the distortion should be.

Simulations to test shape measurement software

Throughout the past decade while the above methods were being developed, lensing simulations designed to test them also evolved. Of particular significance are the shape measurement challenges posed to the weak lensing community as a whole. These blind challenges provide images of simulated sheared galaxies, with the amount of shear unknown to the participants of the challenge. The participants then analyse the images without any preconceptions, thus avoiding *confirmation bias*, and submit an estimate of the shear to the trial organisers. Because the challenge is blind, and because all entrants analyse the same images under the same conditions, the participating methods can be compared and contrasted with each other. So far these trials are limited to shear measurements only, with no flexion applied to the simulated galaxies.

The first such large-scale challenge was the Shear Testing Program (STEP; Heymans et al., 2006a) closely followed by its successor STEP2 (Massey et al., 2007a). The bias of shear measurements was parameterised using a multiplicative bias factor m and an additive factor c:

$$\langle \gamma_i^m \rangle - \gamma_i^t = m_i \gamma_i^t + c_i \tag{1.53}$$

where γ^t is the true (input) shear, γ^m is the measured shear and $i = 1, 2$ represents the component. A negative m thus indicates that the distortion is generally

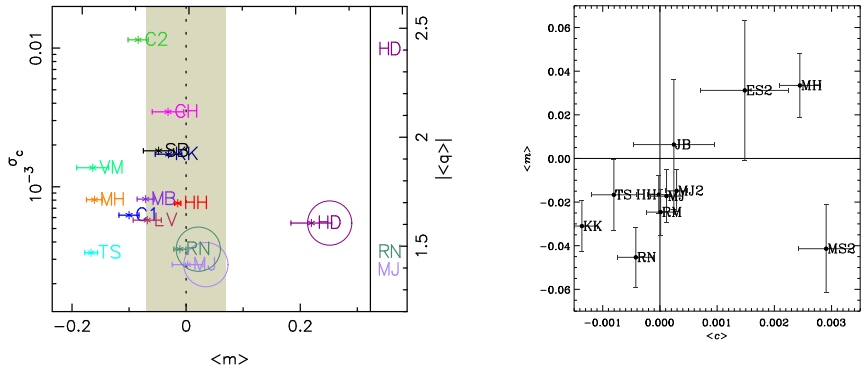

Figure 1.18 Results from STEP (left panel) and STEP2 (right panel) comparing m and c biases for participating methods. Note the difference in scale; the entire figure for STEP2 is within the grey band signifying a calibration bias of less than 7 per cent in the STEP1 figure. The closer to zero a method is, the greater its ability to recover the input shear. Figures originally published in Heymans et al. (2006a) and Massey et al. (2007a); for details on the different methods the reader is referred there.

underestimated, something most entries in STEP suffer from. A systematic offset c may be caused by e.g. insufficient PSF correction but is in general small for implementations in use today. The first STEP installment strived to provide as realistic simulations as possible, while the successor introduced some simplifications to ensure biases were not due to e.g. shape noise. Already in STEP, however, the most successful methods achieved percent-level accuracy (see Figure 1.18) which is sufficient for current weak lensing surveys but needs to reach sub-percentage accuracy in preparation for near future surveys.

The majority of shape measurement methods taking part in the STEP challenges were based on KSB, but by the time the next generation of challenges emerged this picture had changed. These new sets of blind simulations, Gravitational Lensing Accuracy Testing (GREAT08 and GREAT10; Bridle et al., 2009, 2010; Kitching et al., 2010, 2012) had a somewhat different philosophy to STEP. They were aimed not only at the weak lensing community but endeavoured to entice other communities as well, such as computer scientists. Therefore the simulations were stripped down to the core problem of estimating shear and PSF from images, rather than them being as realistic as possible. Furthermore, there were several branches which, although still kept blind for the participants, allowed for a clear picture of which galaxy properties most affect the accuracy of the measurements. The performance of each method was quantified via a quality factor Q which is essentially a combination of the m and c parameters of STEP. The higher the quality factor, the better the method performs. For future surveys, a Q of about 1000 would be ideal, and current methods achieve in general $Q \sim 20$–100. The results from the GREAT08 challenge are shown in Figure 1.19; for the GREAT10 results the reader is referred to Kitching et al. (2012) as the analysis is too extensive to display succinctly here.

There are a vast number of lensing simulations available more or less publicly. STEP and GREAT have the benefit of being able to compare several methods under the same conditions and thus providing a good measure of how well a method can recover lensing distortions in general. They are however

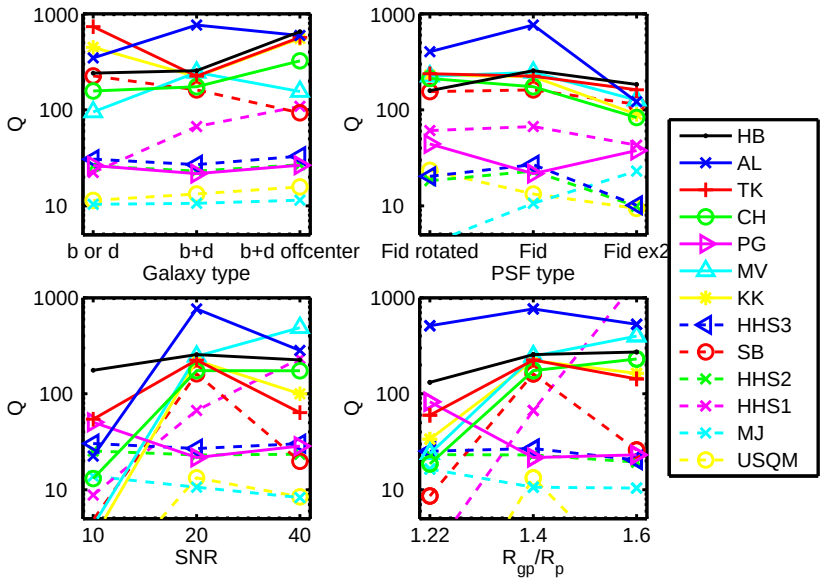

Figure 1.19 Results from GREAT08 showing the Q-values for each branch and each participating method. The higher the Q-value, the better the method performs. Figure originally published in Bridle et al. (2010); for details on the different methods the reader is referred there.

fairly idealised and not attempting to mirror a particular survey. To acquire an accurate impression of how well a method works for a specific survey, simulations imitating the exact observing conditions are necessary. Therefore there are often detailed lensing simulations created for each weak lensing survey. We will, however, always be limited by how well we understand all the effects that influence our distortion measurements, and how closely our simulations mimic reality.

1.4 This Thesis

This Thesis is concerned with studying dark matter haloes using weak lensing through a variety of different applications, observational as well as theoretical. The overall aim is to ascertain how galaxies populate their dark matter haloes, and how the haloes affect the formation and evolution of their host galaxies. To this end we create a new shape measurement pipeline based on the Shapelets formalism with the ability to determine both shear and flexion simultaneously. We also develop software to accurately model the lensing signal on large scales, taking into account contributions from neighbouring and satellite galaxies and galaxy haloes. This extensive software package is then applied to real data, both ground-based and from the Hubble Space Telescope.

In Chapter 2 we describe in detail the shape measurement software known as *the MV pipeline* and show that it is robust using both GREAT08 simulations, and simulations created specifically for the purpose of testing flexion recovery. We then apply it to galaxies which are not monochromatic as is standard in

simulations, but which have a colour gradient. This is something that could potentially be an issue for broad-band imaging, though our findings indicate that the effect is small. Chapter 3 provides the first detection of galaxy-galaxy flexion using data from the Hubble Space Telescope. We use this detection in combination with shear measurements to constrain the density profiles of galaxy-sized haloes, and show that the inclusion of flexion is advantageous to accurately determining the halo mass. In Chapter 4 we describe our halo modelling software and apply it to galaxies in the full CFHTLS survey. We study the halo mass as a function of host galaxy properties such as luminosity and stellar mass. Our constraints on the relations between light and dark matter are tighter than earlier analyses thanks to the large area and depth of the CFHTLS survey. Finally in Chapter 5 we investigate the mass distribution in clusters of galaxies and how it translates into shear and flexion profiles when averaged over several clusters. In clusters we are in general unable to accurately determine the true gravitational center, but are compelled to use visible tracers such as the brightest cluster galaxy to estimate it. As a result the observed density profile is offset from the true profile. We provide predictions for what we expect to observe when several randomly offset profiles are averaged, in shear and flexion space. Furthermore, we show that the use of flexions is particularly valuable in this application.